DATA-DRIVEN APPROACH FOR RUBBERLIKE MATERIALS

A THESIS SUBMITTED TO
THE GRADUATE SCHOOL OF NATURAL AND APPLIED SCIENCES
OF
MIDDLE EAST TECHNICAL UNIVERSITY

BY

MURAT ENIS TUFEKCIOGLU

IN PARTIAL FULFILLMENT OF THE REQUIREMENTS
FOR
THE DEGREE OF MASTER OF SCIENCE
IN
MICRO AND NANOTECHNOLOGY

NOVEMBER 2022

Approval of the thesis:

DATA-DRIVEN APPROACH FOR RUBBERLIKE MATERIALS

submitted by **MURAT ENIS TUFEKCIOGLU** in partial fulfillment of the requirements for the degree of **Master of Science in Micro and Nanotechnology Department, Middle East Technical University** by,

Prof. Dr. Halil KALIPÇILAR
Dean, Graduate School of **Natural and Applied Sciences** _____

Prof. Dr. Deniz ÜNER
Head of Department, **Micro and Nanotechnology** _____

Assoc. Prof. Dr. Hüsnü DAL
Supervisor, **Micro and Nanotechnology, METU** _____

Examining Committee Members:

Prof. Dr. Haluk DARENDELİLER
Mechanical Engineering, METU _____

Assoc. Prof. Dr. Hüsnü DAL
Mechanical Engineering, METU _____

Prof. Dr. Serkan DAĞ
Mechanical Engineering, METU _____

Assoc. Prof. Dr. Ercan GÜRSES
Aerospace Engineering, METU _____

Assist. Prof. Dr. Mehmet Okan GÖRTAN
Mechanical Engineering, Hacettepe University _____

Date:

I hereby declare that all information in this document has been obtained and presented in accordance with academic rules and ethical conduct. I also declare that, as required by these rules and conduct, I have fully cited and referenced all material and results that are not original to this work.

Name, Surname: Murat Enis Tufekcioglu

Signature :

ABSTRACT

DATA-DRIVEN APPROACH FOR RUBBERLIKE MATERIALS

Tufekcioglu, Murat Enis
M.S., Department of Micro and Nanotechnology
Supervisor: Assoc. Prof. Dr. Hüsnü DAL

November 2022, 80 pages

Rubberlike materials, due to their structure, can undergo very high strains during loading and exhibit highly non-linear behavior. After the load is removed, they usually return to their pre-deformation shape, in a sense, no energy is lost during their deformation. Due to these properties, rubberlike materials can be modeled as hyperelastic materials. The modeling approach of many people dealing with rubber is to choose one of the appropriate free energy/strain energy functions developed for rubber in the literature. Material parameter values of the chosen model are determined from the parameter sets that give the best fit to the material tests. Sometimes to find the best-fitted model, several models are checked and compared. Currently, there are over 40 free energy functions defined in the literature and new ones are added to them every day. Finding the best-fitted model can become a tiresome process and data-driven material models can become very useful tools in this context. Thanks to the general approach they offer, they can enable easy and accurate modeling for rubberlike materials that exhibit very different behavior characteristics according to their chemical structure, curing process, additives, and the ambient conditions in which they are used.

Data-driven hyperelasticity is a promising approach for the constitutive modeling of

rubberlike materials because it enables the direct use of experimental data for the construction of the stress-strain response without using any specific analytical expression for the strain energy density function. In this thesis, distinct kinematic approaches to the hyperelastic response of rubberlike materials are proposed based on invariant and principal stretch based formulations given in [1]. Instead of defining a strain energy function with physically meaningful material parameters, the partial derivatives of the strain energy density functions, which are used in stress expressions, are replaced with appropriate B-spline interpolations. Those B-spline interpolations have a set of control points that are defined from various multiaxial loading scenarios such as uniaxial tension, pure shear, and (equi)biaxial tension deformations. These control points can also be defined as parameters of the data-driven material model. The convexity requirement is also enforced through those control points to ensure a convex and stable constitutive response.

The thesis starts with the definitions of B-splines with different degrees and different control points and continues with the introduction of the developed B-spline algorithm. In the sequel, different kinematic approaches to be adopted in data-driven modeling are explained. The proposed data-driven models for each kinematic approach are tested and compared for different degrees and control point numbers using Kawabata and Treloar data sets. Finally, the success of the proposed models in capturing the mechanical behavior for different deformation modes and strain levels is demonstrated by the quality of fit criteria.

Keywords: data-driven approach, hyperelastic material modeling, b-spline generation, invariant based material modeling,optimization

ÖZ

KAUÇUK GİBİ MALZEMELER İÇİN VERİ ODAKLI YAKLAŞIM

Tufekcioglu, Murat Enis
Yüksek Lisans, Mikro ve Nanoteknoloji Bölümü
Tez Yöneticisi: Doç. Dr. Hüsnü DAL

Kasım 2022 , 80 sayfa

Kauçuk benzeri malzemeler, yapıları gereği yükleme sırasında çok yüksek gerilimlere maruz kalabilir ve doğrusal olmayan davranışlar sergileyebilir. Maruz kaldıkları yükü kaldırdıktan sonra, genellikle deformasyon öncesi şekillerine geri dönebilirler, bir anlamda deformasyonları sırasında enerji kaybı olmaz. Bu özelliklerinden dolayı kauçuk benzeri malzemeler hiperelastik malzemeler olarak modellenebilir. Kauçuk ile uğraşan birçok kişinin modelleme yaklaşımı, literatürde kauçuk için geliştirilmiş uygun serbest enerji/gerinim enerjisi fonksiyonlarından birini seçmektir. Seçilen modelin malzeme parametre değerleri, malzeme testlerine en iyi uyumu veren parametre setlerinden belirlenir. Bazen en uygun modeli bulmak için birkaç model kontrol edilir ve karşılaştırılır. Halihazırda literatürde 40'ın üzerinde tanımlı serbest enerji fonksiyonu bulunmaktadır ve bunlara her geçen gün yenileri eklenmektedir. En uygun modeli bulmak yorucu bir süreç olabilir. Veriye dayalı malzeme modelleri bu bağlamda çok faydalı araçlar haline gelebilir. Sundukları genel yaklaşım sayesinde kimyasal yapıları, kürleşme süreçleri, katkı maddeleri ve kullanıldıkları ortam koşullarına göre çok farklı davranış özellikleri sergileyen kauçuk benzeri malzemelerin kolay ve doğru bir şekilde modellenmesini sağlarlar.

Veriye dayalı hiperelastik modelleme, gerinim enerjisi yoğunluk fonksiyonu için herhangi bir özel analitik ifade kullanmadan gerilim-gerinim yanıtının oluşturulması için deneysel verilerin doğrudan kullanımına olanak sağladığından, kauçuk benzeri malzemelerin modellemesi için umut verici bir yaklaşımdır. Bu tezde, [1]'de verilen değişmezler ve asal gerilmelere dayalı formülasyonlar temel alınarak, kauçuk benzeri malzemelerin hiperelastik yanıtına farklı kinematik yaklaşımlar önerilmiştir. Fiziksel olarak anlamlı malzeme parametreleriyle bir gerinim enerjisi fonksiyonu tanımlamak yerine, gerilim ifadelerinde kullanılan gerinim enerjisi yoğunluk fonksiyonlarının kısmi türevleri, uygun B-spline enterpolasyonlarıyla değiştirilmiştir. Bu B-spline enterpolasyonları, tek eksenli çekme, saf kesme ve (eş)çift eksenli çekme gibi çeşitli çok eksenli yükleme senaryolarından tanımlanan bir dizi kontrol noktasına sahiptir. Bu kontrol noktaları, veriye dayalı malzeme modelinin parametreleri olarak da tanımlanabilir. Aynı zamanda kararlı model yanıtını için sağlanması gereken dışbükey gerekliliği bu kontrol noktaları aracılığıyla uygulanır.

Bu tez, farklı derecelere ve farklı kontrol noktalarına sahip B-spline'ların tanımları ile başlar ve geliştirilen B-spline algoritmasının tanıtılmasıyla devam eder. Devamında, veriye dayalı modellemede benimsenecek farklı kinematik yaklaşımlar açıklanmaktadır. Her kinematik yaklaşım için önerilen veri odaklı modeller, Kawabata ve Treloar veri setleri kullanılarak farklı dereceler ve kontrol noktası sayıları için test edilmiş ve karşılaştırılmıştır. Son olarak, önerilen modellerin farklı deformasyon modları ve gerinim seviyeleri (düşük, orta ve yüksek) için mekanik davranışı yakalamadaki başarısı, uygunluk kriterlerinin kalitesi ile gösterilmektedir.

Anahtar Kelimeler: veriye dayalı yaklaşım, hiperelastik malzeme modelleme, b-spline üretimi, değişmez tabanlı malzeme modelleme, optimizasyon

To my beloved wife, our baby daughter, and my family...

ACKNOWLEDGMENTS

First of all, I would like to express my respect and gratitude to my supervisor, Assoc. Prof. Dr. Hüsnü Dal, for his patience and guidance during the study. Even though our paths crossed with him later in my master's education, I had no difficulty in adapting to his team thanks to him.

It was a very enjoyable experience to be in the computational micromechanics laboratory team, they taught me very good information in all meetings in this team, which includes very devoted and successful people in their work. Thanks to the help of the whole team, but especially Alp Kagan Acan, this work was easier than it seemed.

Also, my very special thanks Dr. Funda Aksu Denli and her family, who made this work possible thanks to her high patience and teaching in our virtual meetings that lasted long nights, despite all her busyness and the time zone difference between us.

Finally, I would like to express my deep love and respect to my parents, brother, and sister for their support throughout the thesis writing process. I would also like to thank my dear wife Gülden Ünal Tüfekçioğlu, although she was pregnant throughout most of the process, it was not possible to achieve this result without her patience and support throughout the whole process. My dear daughter Masal Era Tüfekçioğlu, the joy of life and happiness you have given me has been a great support in this process, I love you very much.

TABLE OF CONTENTS

LIST OF TABLES

TABLES

LIST OF FIGURES

FIGURES

LIST OF ABBREVIATIONS

F	Deformation gradient
$\bar{F}$	Modified deformation gradient
C	Right Caucy-Green deformation tensor
$\bar{C}$	Isochoric right Caucy-Green deformation tensor
B	Left Cauchy-Green deformation tensor
N_i(k,d)	Shape function
λ	Stretch
$\bar{\lambda}$	Modified stretch
X	Position of undeformed vector,m
x	Position of deformed vector,m
v	Deformed volume,m^3
V	Undeformed volume,m^3
n	Normal vector of deformed area
N	Normal vector of undeformed area
f	Force acting on a surface for deformed configuration,N
MPa	Mega Pascal
P	First Piola-Kirchoff stress tensor, MPa
σ	Cauchy stress, MPa
S	Second Piola-Kirschoff stress tensor,MPa
$I_{1,2,3}$	Invariants
τ	Kirschoff stress tensor, MPa
$\hat{\tau}$	Isochoric Kirschoff stress tensor, MPa
J	Jacobian determinant
ψ	Free energy function
δ	Kronecker delta
I	Identity tensor
$\hat{p}$	Hydorstatic pressure, MPa
m	Meter

2D	2 Dimensional
3D	3 Dimensional
UT	Uniaxial tension
ET	Equibiaxial tension
PS	Pure shear
BE	Biaxial tension
QOF	Quality of fit
WYPIWYG	What-You-Prescribed-Is-What-You-Get
B-spline	Basis spline
FMINCON	Find a minimum of a constrained nonlinear multivariable function
$\mathscr{B}_0$	Unloaded body
$\mathscr{B}$	Loaded body
R^3	3D Euclidean Space
ν	Areal stretch
λ_{1e}	Experimental results of λ_1
λ_{1f}	Fitted results of λ_1

CHAPTER 1

INTRODUCTION

The models used for rubberlike materials in the literature are divided into phenomenological and micromechanical models. Recently, data-driven modeling has been added to these as a new modeling approach. Data-driven models have attracted attention because they easily overcome the difficulties of phenomenological and micromechanical models. Data-driven modeling is also promising in terms of the variety of its application area. This work will likely be a milestone for modeling metamaterials or non-traditional materials that are new to the materials literature because it may be possible to model these materials similarly. In the last decades, there are various data-driven methods have been proposed. These methods can be classified into two main groups; (i) model-free distance-minimizations based data-driven and (ii)model-based data-driven methods. The study conducted here uses a model-based data-driven approach. Strain energy is said to be a function of invariants or principal stretches without giving any precise formulation or definition. Instead of defining a strain energy function, partial derivatives of the strain energy with respect to invariants, principal stretches, or according to model parameters, which are functions of invariants and principal stretches, are defined with B-splines. The use of the test data determines B-splines with suitable control points. For all four kinematic approaches, model parameters have no physical meaning. Thus, models are mainly general and can be applied to different kinds of rubber.

1.1 Motivation and Problem Definition

Rubber is a material that can be classified as hyperelastic material when the observed strain behavior under stress is investigated. Originally latex is a white liquid from a

tree named $Hevea\,brasiliensis$. The processed latex from the tree can develop as natural rubber. Rubber can also be produced synthetically. [2]

The physical properties of rubberlike materials can be defined by their very high deformability and complete recoverability. Rubberlike materials have properties like long chains and increased flexibility and mobility for high deformability. These long-chained molecules should be linked together for full recoverability so that the main structure can recover after deformation [3].

Natural rubber is a polymeric material that has a monomer named $isoprene$. Multiple $isoprene$, which has a chain structure called $polyisoprene$. This polymer can be hardened with sulfur and heat treatment under $140 - 160°C$. This process is named Vulcanization. The main idea behind this process is to develop links between different chains to increase the strength of the rubber. In literature, different modeling approaches and numerous models describe the material's free energy function for predicting rubberlike material behavior. While some approaches use principal stretch and invariant-based mathematical models to predict the material's stress-strain curve, there are also micromechanically based material models that try to imitate the chain structure of rubber with physically meaningful parameters. [1] recently listed 44 hyperelastic models from each group and compared their performances. Most models can predict rubber behavior under certain conditions. While some give good fits for high stretch levels, some can produce agreeable results only for the Gaussian regime of deformations. Due to this diversity, choosing the appropriate model for the rubber material and determining the best parameter set can become challenging. Hence, data-driven models have gained attention to overcome the challenges of the phenomenological and micromechanical models. Generally, data-driven modeling approaches can be classified into two main categories, see [4, 5]. These are; (i) the model-free distance minimization approach and (ii) WYPIWYG (What-You-Prescribed-Is-What-You-Get) approach. Model-free distance minimization was developed to bypass constitutive modeling by finding stress-strain pairs with the least distance to experimental data. This approach was initially proposed for non-linear truss and linear elastic materials [6] and then extended to hyperelastic materials [7] and inelastic materials [8]. WYPIWYG approaches form a constitutive manifold directly from the experimental data. These approaches focus on building constitutive

relations through interpolation functions to describe the free energy function. WYPIWYG approach was developed based on the idea proposed in [9]. Later, WYPIWYG was extended to the macro-micro-macro approach by [10, 11]. Micro-macro-micro approach is a procedure in which micromechanical behavior is obtained from a macroscopic test without an underlying analytical model. Then computed micromechanical behavior is used to predict continuum behavior under any loading condition.

Invariant-based models define the free energy function in terms of Invariant properties of material deformation. Neo-Hookean [12], Yeoah [13], Gent [14], Yeoh-Fleming [15], Mooney-Rivlin [16] [17] are well known examples can be chosen from many. Principal stretch-based models are similar to invariant-based models, but they define the free energy function ψ in principal stretches λ. Well-known literature examples of principal stretch based models can be listed as Valanis-Landel [18], Ogden [19], Shariff [20] and Tube [21] models. Other than these two generic categories, some micromechanics-based models perform well compared to invariant and principal stretch-based models. Famous micromechanics based models can list as, Three-Chain Model [22], Eight-Chain Model(Arruda-Boyce Model) [23], Microsphere Model [24], Extended Eight-Chain Model [25] [26]. There are also many other models and categories, including Mixed Invariant and Principal Stretch Based models. For further reading, [1] is a precious source to understand and compare models in the literature.

1.2 Proposed Methods and Models

Rubberlike materials are modeled through a strain energy density function that depends on either principal stretches or invariants. Hence, the notion of material objectivity and material frame indifference are *a priori* satisfied. In the sequel, we propose four different data-driven approaches that depend (i) directly and (ii) indirectly on invariants and principal stretches.

The goal is to obtain a data-driven constitutive framework that can give accurate predictions for all deformation ranges and states, such as uniaxial tension, biaxial tension, and pure shear deformations. For this purpose, only the partial derivatives of the strain energy density functions are estimated by appropriate B-spline interpola-

tions that eliminate any fixed form of strain energy density function. In this study, all methods must calculate the B-Spline and its shape functions. A generic B-Spline generation tool code is developed and implemented for all models to make it easier. The B-spline tool can predict any curve by using any degree of shape functions and using any number of knots within the range where the curve is defined.

1.3 Contributions and Novelties

The experimental rubber data is obtained from Treloar's [27] experiments and Kawabata's [28] studies. Since both data have been widely used in the literature, the method's success can be compared easily, and results can be discussed more adequately. Treloar's data consists of uniaxial tension, pure shear, and equ-biaxial tension test data for vulcanized rubber. On the other hand, Kawabata provides a biaxial data set. MATLAB's Optimization Toolbox has been used to predict the best fitted control point set. FMINCON is the function that has been used. For the cases with a higher number of parameters which causes divergence for the solution, the number of iterations has been increased to get physical-based results. To understand the effect of the control point number, the quality of the fit study was conducted at the end, and plots were obtained in terms of the number of control points and fit quality.

Although data-driven studies have significantly increased over recent years, the data-driven approach for engineering problems, especially computational mechanics problems, needs to be shared. This rarity is because the data-driven approach may stand far from the physics behind mechanical issues. This study considers physical rules with constraints of optimization solutions.

1.4 The Outline of the Thesis

The thesis is organized as follows. In Chapter 1, a brief introduction to the topic has provided. Chapter 2 focuses on the basics of continuum mechanics, gives definitions of invariants and principal stretches, offers free energy definitions of hyperelastic materials with their related stress expressions, and shows the homogenous deformation modes used for material characterization. Spline definition, Bézier curves, and B-Splines are explained in chapter 3. In chapter 4 new data-driven model with four

different kinematic approaches is proposed. All models are structured with B splines. Finally, chapter 5 summarizes the thesis work.

CHAPTER 2

CONTINUUM MECHANICS BACKGROUND

This section summarizes basic concepts in continuum mechanics and introduces the kinematics and state variables of an isotropic hyperelastic body subjected to finite deformations. Different formulations of the free energy function, governed by principal stretches and invariants, are given with its stress and strain expressions.

2.1 Kinematics

An unloaded body, defined as $\mathscr{B}_0$ is composed of an infinite number of material points. These points occupy geometrical positions in 3D Euclidean Space R^3. Any arbitrary point on the unloaded body can be labeled with its position vector $\boldsymbol{X}$, and its new position on the current state at time t by $\boldsymbol{x}$. The loaded body is defined as $\mathscr{B}$. See Figure 2.1.

With the deformation map $\varphi(\mathbf{X}, t)$ we can represent a nonlinear deformation field within time $t \in \mathscr{T} \subset \mathbb{R}_+$. In this manner, the material points $\mathbf{X} \in \mathscr{B}_0$ can be defined on spatial points $\mathbf{x} = \varphi_t(\mathbf{X})$ which we can call the Eulerian(current) configuration of a material point. Let us use $T_X\mathscr{B}_0$ and $T_x\mathscr{B}$ to symbolize the tangent spaces in the Eulerian and the Lagrangian manifolds. The deformation gradient becomes;

$$\mathbf{F} : T_X\mathscr{B}_0 \to T_x\mathscr{B}; \quad \mathbf{F} := \frac{\partial \varphi_t(\mathbf{X})}{\partial \mathbf{X}} \tag{2.1}$$

Equation 2.1 is used to map the unit tangent of the Lagrangian configuration onto the Eulerian configuration. After that, let $T_X^*\mathscr{B}_0$ and $T_x^*\mathscr{B}$ indicate the cotangent spaces in the Lagrangian and Eulerian manifolds. Volume map det[**F**] is weighed by cof[**F**], and we can describe a normal map per unit reference volume as;

$$\mathbf{F}^{-T} : T_X^*\mathscr{B}_0 \to T_x^*\mathscr{B}; \quad \mathbf{n} = \mathbf{F}^{-T}\mathbf{N} \tag{2.2}$$

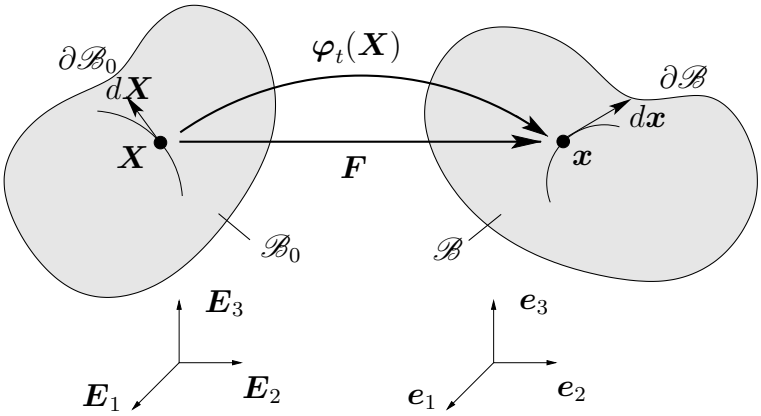

Figure 2.1: Left-hand side is the (unloaded) reference configuration $\mathscr{B}_0$ with a boundary description $\partial\mathscr{B}_0$, right-hand side is the deformed configuration $\mathscr{B}$ with a boundary $\partial\mathscr{B}$ as a result of deformation $\boldsymbol{\varphi}$.

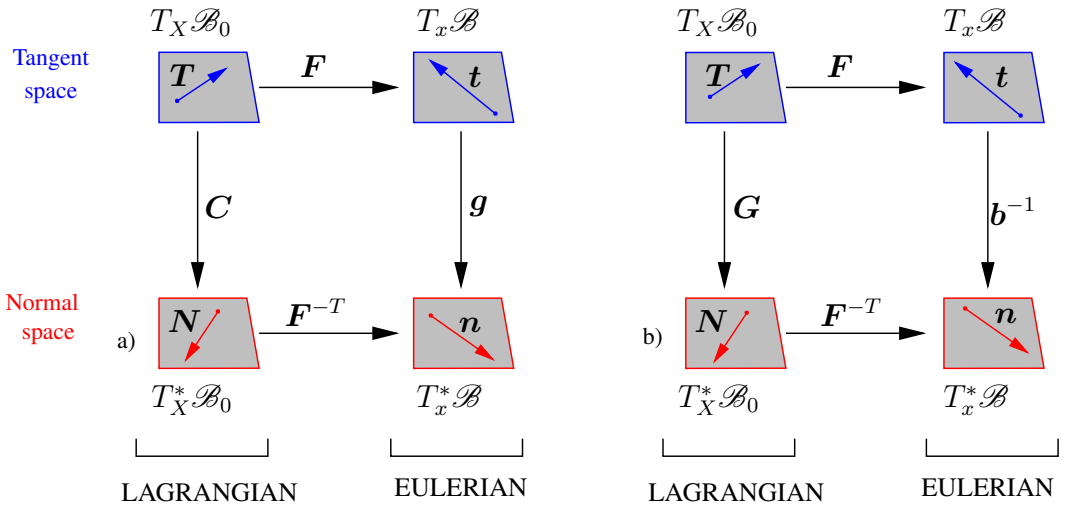

Figure 2.2: Definition of metric tensors. a) current metric in Lagrangian configuration $\boldsymbol{C} = \boldsymbol{F}^T\boldsymbol{g}\boldsymbol{F}$; b) reference metric in Eulerian configuration $\boldsymbol{b}^{-1} = \boldsymbol{F}^{-T}\boldsymbol{G}\boldsymbol{F}^{-1}$

Equation 2.2 is used to map the vector **N** of the Lagrangian configuration onto its counterpart **n** in the Eulerian configuration. In the undeformed configuration, let $d\mathbf{X}$, $d\mathbf{A}$, and dV represent the infinitesimal line, area, and volume elements. Also, the deformation gradient $\boldsymbol{F}$, its cofactor as, cof[**F**] = det[**F**]$\mathbf{F}^{-T}$ and the Jacobian J:=det[**F**]>0 characterize the deformation of infinitesimal line, area, and volume elements

$$d\mathbf{x} = \mathbf{F}d\mathbf{X}, \quad d\mathbf{a} = cof[\mathbf{F}]d\mathbf{A}, \quad dv = det[\mathbf{F}]dV \tag{2.3}$$

To ensure from non penetrable deformations φ, J:=det[**F**] >0 relations should be satisfied. Also, **G** and current **g** metric tensors and respectively $\mathcal{N}_X$ of **X** and $\mathcal{N}_x$ of **x**, should furnish locally $\mathscr{B}_0$ and the spatial $\mathscr{B}$ manifolds. To map between co- and contra-variant objects in Lagrangian and Eulerian manifolds, mentioned metric tensors play a vital role. In light of these definitions, the left Cauchy Green tensor can be written as

$$\mathbf{C} = \mathbf{F}^T\mathbf{g}\mathbf{F} \quad \text{and} \quad \mathbf{c} = \mathbf{F}^{-T}\mathbf{G}\mathbf{F}^{-1} \tag{2.4}$$

the pull back of the current metric $\boldsymbol{g}$ and the inverse of the left Cauchy Green tensor $\boldsymbol{c} = \boldsymbol{b}^{-1}$ is defined as the push-forward of the Lagrangian metric $\boldsymbol{G}$., see Figure 2.2.

2.2 Principal Stretches and Invariants

We can define an energy expression for an isotropic material governed by principal stretches or invariants to fully establish the principle of material objectivity and material frame indifference.

$$\mathbf{C} := \sum_{a=1}^{3} \lambda_a^2 \mathbf{N}^a \otimes \mathbf{N}^a \quad \text{and} \quad cof[\mathbf{C}] := \sum_{a=1}^{3} \nu_a^2 \mathbf{N}^a \otimes \mathbf{N}^a \tag{2.5}$$

where

$$\nu_i = J/\lambda_i \quad \text{with} \quad \nu_1 = \lambda_2\lambda_3, \quad \nu_2 = \lambda_3\lambda_1, \quad \nu_3 = \lambda_1\lambda_2 \tag{2.6}$$

are the definition of principal areal stretches given in Figure 2.3 .

Three isotropic invariants of the right Cauchy Green tensor can be defined as

$$I_1 := tr[\mathbf{C}], \quad I_2 := tr[cof[\mathbf{C}]], \quad \text{and} \quad I_3 := det[\mathbf{C}] \tag{2.7}$$

When we compare expressions 2.3 and 2.7, we can easily conclude that these invariant definitions are affiliated with $volumetric$, $areal$, and $linear$ stretches within an

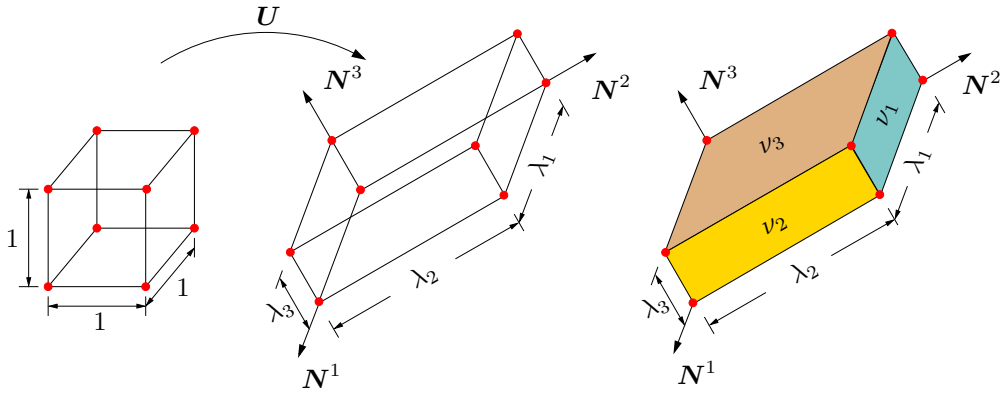

Figure 2.3: The invariants (a) Undeformed infinitesimal unit volume element (b) Deformed element where $\boldsymbol{N}^1$, $\boldsymbol{N}^2$ and $\boldsymbol{N}^3$ are the principal directions in the Lagrangian setting. (i) $I_1(\boldsymbol{C}) = \lambda_1^2 + \lambda_2^2 + \lambda_3^2$ as sum of squares of the principal stretches, (ii) $I_2(\boldsymbol{C}) = \nu_1^2 + \nu_2^2 + \nu_3^2$ as sum of squares of principal areal stretches where $\nu_i = J/\lambda_i$ and (iii) $I_3 = J^2 = \lambda_1^2\lambda_2^2\lambda_3^2$ as square of volumetric stretch.

infinitesimally small cube which represents the material properties. The deformation gradient $\mathbf{F}$ can be broken down into volumetric and unimodular parts, respectively, $\boldsymbol{F}_{vol} := J^{1/3}\mathbf{1}$ and $\bar{\boldsymbol{F}} := J^{-1/3}\boldsymbol{F}$ as,

$$\mathbf{F} = \mathbf{F}_{\boldsymbol{vol}}\bar{\boldsymbol{F}} \tag{2.8}$$

2.3 The Free Energy Function

Along with the multiplicative split of the deformation gradient 2.8, a special class of materials in finite elasticity is governed by the free energy function of the form;

$$\psi(\boldsymbol{F}) = \psi(J) + \psi(\bar{\boldsymbol{F}}) \tag{2.9}$$

which dates back to Flory [29]. The original proposition of Flory was in an additive form

$$\psi(\theta, \mathbf{F}) = \psi_v(\theta, J) + \psi_e(\theta, \mathbf{F}) \tag{2.10}$$

where the first term $\psi(\theta, J)$ represents inter-molecular interactions occurring in simple liquids, and the terms of the function are the temperature θ and volume change J. The second therm $\psi(\theta, F)$, also has similar dependencies on the total deformation and temperature, and this term represents entropic shape changes in the material.

So, we can say that even if it is small, the entropic effect on the volumetric response is also included in the energy function expression. Nevertheless, it can be counted as the standard approach in the rubber elasticity community that uses exact geometrical decomposition of additive form in equation 2.9 with the deformation gradient into unimodular and volumetric parts with multiplicative split 2.8. [30–34]. Although within the incompressibility limit, both approaches are likely to have the same constitutive conclusion, Dal's work [35] shows that it becomes more realistic when we treat it as slightly compressible elastomers, and this approach originated from Flory. The compressibility of rubber can be explained before the macroscopic cracks which occurred while the degradation of the material, with the small cavities, introduced while manufacturing [36]. Furthermore, splitting perfectly geometric should be eliminated to prevent computational cost and instantaneous Poisson's ratio at the boundary conditions. In this manner, examples of pure volumetric free energy functions are defined in Kadapa, and Hossain's work [37]. With the help of these examples, the main goal of reaching boundary behaviors along convexity - quasi-incompressible behavior- and growth requirements would achieve.

2.4 Stress Expressions

The most fundamental requirement of hyperelasticity is a free energy function defined in two forms as written in equations 2.9 and 2.10. In general hyperelastic materials are assumed to have no dissipation, resulting in a canonical relationship within the energy function between Lagrangian and Eulerian stresses.

$$\mathbf{S} = 2\partial_{\boldsymbol{C}}\hat{\psi}(\mathbf{F}^T\mathbf{g}\mathbf{F}, \mathbf{X}) \quad \text{and} \quad \boldsymbol{\tau} = 2\partial_{\boldsymbol{g}}\tilde{\psi}(\mathbf{g}, \mathbf{F}, \mathbf{X}) \tag{2.11}$$

In equation 2.11, $\boldsymbol{S}$ represents the second Piola–Kirchhoff, and $\boldsymbol{\tau}$ represents the Kirchhoff stresses. The $\boldsymbol{\tau}$ expression is also named the Doyle–Eriksen formula of hyperelasticity. We can relate isotropic finite elastic materials with principal stretches or invariants with;

$$\psi = \tilde{\psi}(\lambda_1, \lambda_2, \lambda_3) \quad \text{or} \quad \psi = \tilde{\psi}(I_1, I_2, I_3) \tag{2.12}$$

Which is validated by the principle of material objectivity and material frame invariance.

2.4.1 Invariant Formulations

With the help of the chain rule, the Lagrangian and Eulerian stress expression can be represented as with the initial equation 2.12_2;

$$\mathbf{S} = 2\partial_{\mathbf{C}}\psi = 2\left[\frac{\partial\psi}{\partial I_1}\frac{\partial I_1}{\partial \mathbf{C}} + \frac{\partial\psi}{\partial I_2}\frac{\partial I_2}{\partial \mathbf{C}} + \frac{\partial\psi}{\partial I_3}\frac{\partial I_3}{\partial \mathbf{C}}\right] \tag{2.13}$$

$$\boldsymbol{\tau} = 2\partial_{\boldsymbol{g}}\psi = 2\left[\frac{\partial\psi}{\partial I_1}\frac{\partial I_1}{\partial \boldsymbol{g}} + \frac{\partial\psi}{\partial I_2}\frac{\partial I_2}{\partial \boldsymbol{g}} + \frac{\partial\psi}{\partial J}\frac{\partial J}{\partial \boldsymbol{g}}\right] \tag{2.14}$$

We need to define the following derivatives to move further the expressions of the Lagrangian and Eulerian stress tensors, which are described in equations 2.13 and 2.14;

$$\partial_{\boldsymbol{C}} I_1 = \mathbf{1}, \quad \partial_{\boldsymbol{C}} I_2 = I_1\mathbf{1} - \mathbf{C}, \quad \partial_{\boldsymbol{C}} J = \frac{1}{2}J\mathbf{C}^{-1} \tag{2.15}$$

The same approach is also needed from the push forward expression of 2.15 for the spatial metric **g**, so,

$$\partial_{\boldsymbol{g}} I_1 = \mathbf{b}, \quad \partial_{\boldsymbol{g}} I_2 = I_1\mathbf{b} - \mathbf{b}^2, \quad \partial_{\boldsymbol{g}} J = \frac{1}{2}J\mathbf{g}^{-1} \tag{2.16}$$

We can insert 2.15 and 2.16 into 2.13 and 2.14. After rearrangement, we can finally get the invariant-based stress relation solution for isotropic hyperelastic materials.

$$\text{with} \quad c_1 = \frac{\partial\psi}{\partial I_1} \quad c_2 = \frac{\partial\psi}{\partial I_2} \quad p = -J\partial_J\psi \tag{2.17}$$

We can merge and generalize the equations 2.13 and 2.14 within the principal directions. Note that this expression is based on principal stretches;

$$\boxed{\begin{aligned} S_i &= 2(c_1 + I_1 c_2)1 - 2c_2\lambda_i^2 - \frac{1}{\lambda_i^2}p \\ \tau_i &= 2(c_1 + I_1 c_2)\lambda_i^2 - 2c_2\lambda_i^4 - pg^{-1} \end{aligned}} \tag{2.18}$$

2.4.2 Principal Stretch Based Formulations

To get a principal stretch-based free energy function 2.12_1, the Kirchoff stress tensor can be written as;

$$\boxed{\begin{aligned} \mathbf{S} &= \sum_{a=1}^{3}\frac{1}{\lambda_a}\beta_a\mathbf{N}_a \otimes \mathbf{N}_a - p\mathbf{C}^{-1} \\ \boldsymbol{\tau} &= \sum_{a=1}^{3}\lambda_a\beta_a\mathbf{n}_a \otimes \mathbf{n}_a - p\mathbf{1} \end{aligned}} \tag{2.19}$$

with

$$\beta_1 = \frac{\partial\psi}{\partial\lambda_1} \quad \beta_2 = \frac{\partial\psi}{\partial\lambda_2} \quad \beta_3 = \frac{\partial\psi}{\partial\lambda_3} \tag{2.20}$$

2.4.3 Stresses Under Homogeneous Deformations

Since most of the experiments are done with a displacement-focused setup, most of the time, only easier data taken from the experiments become the nominal stress, and the cross-section area measurement is pretty rare. So we can define the deformation gradients and the stress expressions as the following base expressions and definitions.

- $Uniaxial\ Tension$
- $Equibiaxial\ Tension$
- $Pure\ Shear$
- $Biaxial\ Tension$

$$\mathbf{F} = \begin{bmatrix} F_{11} & 0 & 0 \\ 0 & F_{22} & 0 \\ 0 & 0 & F_{33} \end{bmatrix} \text{ and } \mathbf{P} = \begin{bmatrix} P_1 & 0 & 0 \\ 0 & P_2 & 0 \\ 0 & 0 & P_3 \end{bmatrix} \tag{2.21}$$

$Uniaxial\ tension$: For an incompressible hyperelastic solid, the deformation and stress state under uniaxial tension are given in Figure 2.4 and equation 2.22.

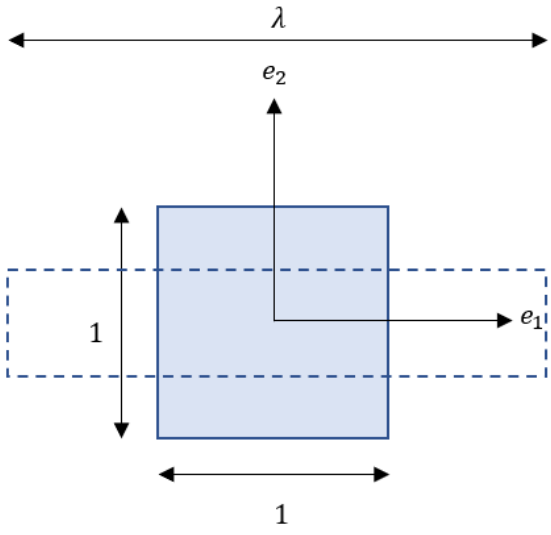

Figure 2.4: Uniaxial tension deformation

$$\mathbf{F} = \begin{bmatrix} \lambda & 0 & 0 \\ 0 & \frac{1}{\sqrt{\lambda}} & 0 \\ 0 & 0 & \frac{1}{\sqrt{\lambda}} \end{bmatrix} \text{ and } \mathbf{P} = \begin{bmatrix} P_1 & 0 & 0 \\ 0 & 0 & 0 \\ 0 & 0 & 0 \end{bmatrix} \tag{2.22}$$

The first two invariants under uniaxial deformation are written as;

$$I_1 = \lambda^2 + \frac{2}{\lambda}, \quad I_2 = 2\lambda + \frac{1}{\lambda^2} \tag{2.23}$$

The nominal stress $\mathbf{P} = \mathbf{FS}$ expression under uniaxial tension deformation state for invariant and principal stretch-based formulations read.

(UT)	Invariant:	$P_1 = 2(c_1 + \frac{c_2}{\lambda})(\lambda - \frac{1}{\lambda^2})$
(UT)	Prin. stretch:	$P_1 = \beta_1 - \frac{1}{\lambda^{3/2}}\beta_2$

(2.24)

Equibiaxial tension : For an incompressible hyperelastic solid, the deformation and stress state under equibiaxial tension are given in Figure 2.5 and equation 2.25.

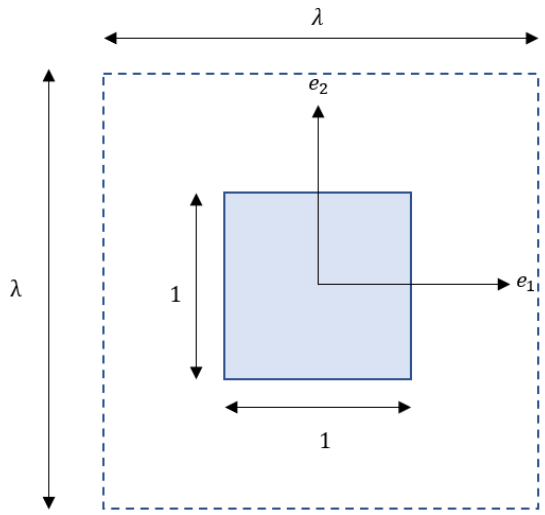

Figure 2.5: Equibiaxial tension deformation

$$\mathbf{F} = \begin{bmatrix} \lambda & 0 & 0 \\ 0 & \lambda & 0 \\ 0 & 0 & \frac{1}{\lambda^2} \end{bmatrix} \text{ and } \mathbf{P} = \begin{bmatrix} P_1 & 0 & 0 \\ 0 & P_1 & 0 \\ 0 & 0 & 0 \end{bmatrix} \tag{2.25}$$

The first two invariants under the equibiaxial deformation state read.

$$I_1 = 2\lambda^2 + \frac{1}{\lambda^4}, \quad I_2 = \lambda^4 + \frac{2}{\lambda^2} \quad . \tag{2.26}$$

The nominal stress under equibiaxial tension is read for invariant and principal stretch-based formulations.

(ET)	Invariant:	$P_1 = 2(c_1 + c_2\lambda^2)(\lambda - \frac{1}{\lambda^5})$
(ET)	Prin. stretch:	$P_1 = \beta_1 - \frac{1}{\lambda^3}\beta_2$

(2.27)

Biaxial tension : For an incompressible hyperelastic solid, the deformation and stress state under biaxial tension are given in Figure 2.6 and equation 2.28.

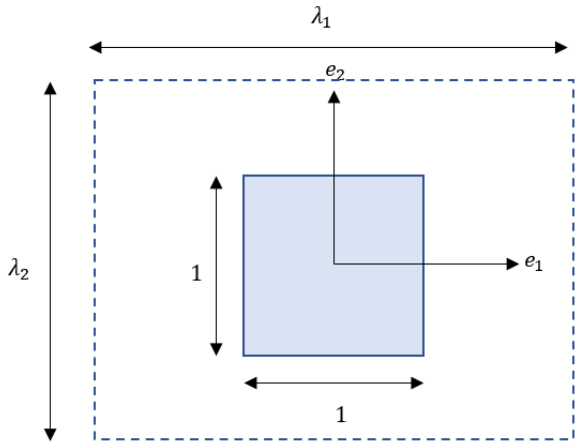

Figure 2.6: Biaxial tension deformation

$$\mathbf{F} = \begin{bmatrix} \lambda_1 & 0 & 0 \\ 0 & \lambda_2 & 0 \\ 0 & 0 & \frac{1}{\lambda_1\lambda_2} \end{bmatrix} \text{ and } \mathbf{P} = \begin{bmatrix} P_1 & 0 & 0 \\ 0 & P_2 & 0 \\ 0 & 0 & 0 \end{bmatrix} \tag{2.28}$$

The first two invariants under the biaxial deformation state read.

$$I_1 = \lambda_1^2 + \lambda_2^2 + \frac{1}{\lambda_1^2\lambda_2^2}, \quad I_2 = \lambda_1^2\lambda_2^2 + \frac{1}{\lambda_1^2} + \frac{1}{\lambda_2^2} \tag{2.29}$$

The nominal stress under biaxial tension is read for invariant and principal stretch-based formulations.

$$\begin{array}{lll} \text{(BT)} & \text{Invariant:} & P_1 = 2(c_1 + c_2\lambda_2^2)(\lambda_1 - \frac{1}{\lambda_1^3\lambda_2^2}) \\ & & P_2 = 2(c_1 + c_2\lambda_1^2)(\lambda_2 - \frac{1}{\lambda_1^2\lambda_2^3}) \\ \text{(BT)} & \text{Prin. stretch:} & P_1 = \beta_1 - \frac{\beta_3}{\lambda_1\lambda_2^2} \\ & & P_2 = \beta_2 - \frac{\beta_3}{\lambda_1^2\lambda_2} \end{array} \tag{2.30}$$

Pure shear : For an incompressible hyperelastic solid, the deformation and stress state under pure shear are given in Figure 2.7 and equation 2.31.

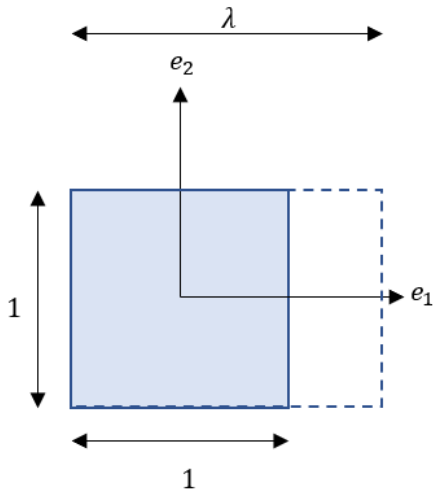

Figure 2.7: Pure shear deformation

$$\mathbf{F} = \begin{bmatrix} \lambda & 0 & 0 \\ 0 & 1 & 0 \\ 0 & 0 & \frac{1}{\lambda} \end{bmatrix} \text{ and } \mathbf{P} = \begin{bmatrix} P_1 & 0 & 0 \\ 0 & P_2 & 0 \\ 0 & 0 & 0 \end{bmatrix} \tag{2.31}$$

The first two invariants under the pure shear deformation state read.

$$I_1 = I_2 = \lambda^2 + \frac{1}{\lambda^2} + 1 \tag{2.32}$$

The nominal stress under pure shear for invariant and principal stretch-based formulations read.

$$\boxed{\begin{array}{lll} \text{(PS)} & \text{Invariant:} & P_1 = 2(c_1 + c_2)(\lambda - \frac{1}{\lambda^3}) \\ & & P_2 = 2(c_1 + c_2\lambda^2)(1 - \frac{1}{\lambda^2}) \\ \text{(PS)} & \text{Prin. stretch:} & P_1 = \beta_1 - \frac{\beta_3}{\lambda^2} \\ & & P_2 = \beta_2 - \frac{\beta_3}{\lambda^2} \end{array}} \tag{2.33}$$

CHAPTER 3

SPLINES

In this chapter theory behind splines and spline generation and B-splines will be explained.

3.1 Introduction

Splines are special piecewise functions that generate a polynomial. Splines are mainly used for data interpolation or smoothing. The main idea behind splines is that instead of representing a curve with a more significant ordered single function, it is represented with a lower ordered piecewise function set and vertices. This approach is easier to solve.

3.2 Bézier Curve

B-Splines can be represented by with parametric equation combination of Bézier curves. A parameter, t is used to determine the value of a point on the curve, where $0 \leq t \leq 1$. An example of a first degree Bézier curve is given in Figure 3.1 where P_0 and P_1 are the control points of the Bézier curve. The parametric definition of the line between P_0 and P_1 is given as;

$$P_0 = (x_0, y_0), \quad P_1 = (x_1, y_1), \quad \text{and} \quad P(x, y) = P(t) = (1-t)P_0 + tP_1 \tag{3.1}$$

with

$$x(t) = (1-t)x_0 + tx_1 \qquad y(t) = (1-t)y_0 + ty_1 \tag{3.2}$$

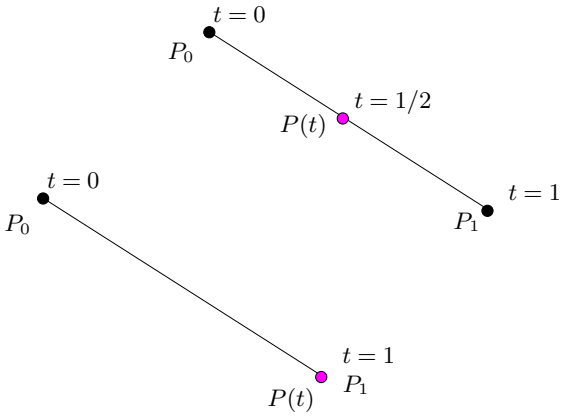

Figure 3.1: Example Bézier curve with 1^{st} degree

We can list some properties of Bézier curves as;

- Parameter t represents the location of the point $P(t)$ on the line between P_0 and P_1.
- An n degree Bézier curve is defined using $n + 1$ control points.
- The first and the last control points are always the endpoints of the Bézier curve.
- To define a quadratic Bézier curve as shown in Figure 3.2 three control points P_0, P_1 and P_2 are needed. Two line equations between $P_0 \rightarrow P_1$ and $P_1 \rightarrow P_2$ are given as;

$$Q_0(t) = (1-t)P_0 + tP_1 \qquad Q_1(t) = (1-t)P_1 + tP_2 \tag{3.3}$$

- $C(t)$ is a point (shown by black dots in the Figure 3.2) on the quadratic Bézier curve that lies on the line $Q_0 \rightarrow Q_1$ (blue line in the same figure)

$$C(t) = (1-t)Q_0 + tQ_1 = (1-t^2)P_0 + 2t(1-t)P_1 + t^2P_2 \tag{3.4}$$

- A Bézier curve is contained within its control polygon, defined as the "Convex hull property" of a Bézier curve. For a quadratic Bézier curve, the control polygon is shown with red lines in Figure 3.2.

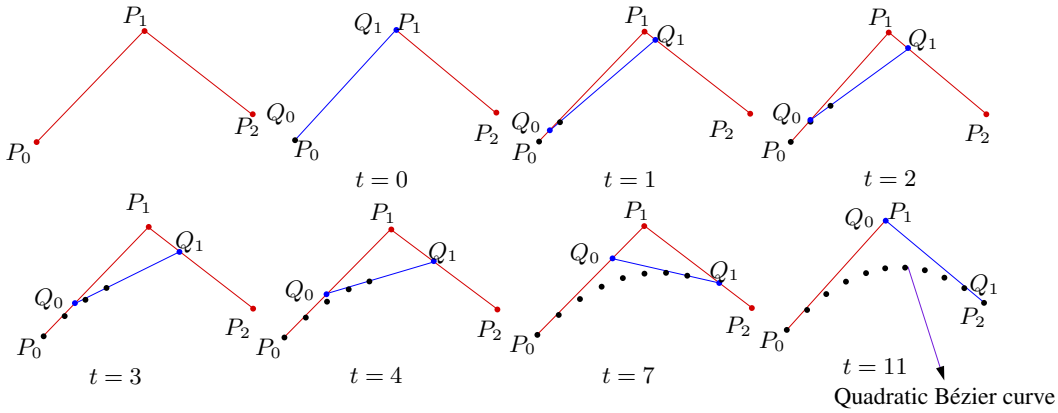

Figure 3.2: Formation of Bézier curve

3.2.1 Bernstein polynomials

The binomial expansion reads

$$1 = (u + (1-u)^n) = \sum_{i=0}^{n} \binom{n}{i} u^i (1-u)^{n-i}. \tag{3.5}$$

Bernstein polynomials with degree n can be defined as

$$B_i^n(u) = \binom{n}{i} u^i (1-u)^{n-i}, \quad i = 0, ..., n \tag{3.6}$$

Where n is the degree of the Bernstein polynomials and $n+1$ is the number of the Bernstein polynomials for the corresponding segment. Properties of Bernstein polynomials can be listed as; Bernstein polynomials are symmetric,

$$B_i^n(u) = B_{n-i}^n(1-u) \tag{3.7}$$

Their only roots are at 0 and 1,

$$B_i^n(0) = B_{n-i}^n(1) = \begin{cases} 1 & \text{for} \quad i = 0 \\ 0 & \quad\quad\;\; i > 0 \end{cases} \tag{3.8}$$

They form a partition of unity,

$$\sum_{i=0}^{n} B_i^n(u) = 1, \quad \text{for all} \quad u \in \mathbb{R} \tag{3.9}$$

They are always positive,

$$B_i^n(u) > 0, \quad for \quad u \in (0,1) \tag{3.10}$$

Higher ordered polynomials can be calculated with the recursion formula

$$B_i^n + 1(u) = uB_i - 1^n(u) + (1-u)B_i^n(u), \tag{3.11}$$

This recursion pattern can be represented as follows;

$$\begin{array}{ccccc} B_0^0 & B_0^1 & B_0^2 & ... & B_0^n \\ & B_1^1 & B_1^2 & ... & B_1^n \\ & & B_2^2 & ... & B_2^n \\ & & & \ddots & \vdots \\ & & & & B_n^n \end{array} \tag{3.12}$$

where $B_0^0 = 1$ and any other B values that cannot be represented in this pattern are 0.

3.2.2 Bézier Representation

Every polynomial $P(u)$ with the degree of d can be represented with a unique n^{th} degree Bézier representation. If and only if $d \leq n$.

$$b(u) = \sum_{i=0}^{n} c_i B_i^n(u) \tag{3.13}$$

One can also extend this representation with parameter transformation

$$u = a(1-t) + bt, \quad a \neq b \tag{3.14}$$

and

$$P(u(t)) = \sum_{i=0}^{n} b_i B_i^n(t) \tag{3.15}$$

The set b_i is called Bézier points or, more generally, vertices of Bézier curve P(u) over [a,b]. Bernstein polynomials are symmetric, so that we can say that.

$$P(u) = \sum_{i=0}^{n} b_i B_i^n(t) = \sum_{i=0}^{n} b_{n-i} B_i^n(s) \tag{3.16}$$

where

$$u = a(1-t) + bt = b(1-s) + as \tag{3.17}$$

This relation shows that we can define Bézier over [a,b] and [b,a] with two different parameter orientations. For the endpoints of the Bézier curve segment P[a,b], always

$$b(a) = b_0 \quad \text{and} \quad b(b) = b_n \tag{3.18}$$

3.3 B-Splines

Splines are piecewise curves that are differentiable up to a prescribed order. The simplest example is a piecewise linear C^0 spline, i.e., a polygonal curve. The name splines come from elastic beams that lay out sweeping curves in ship design.

A curve $C(t)$ is called spline of degree n with the knots $t_0, ..., t_m$ where $t_i \leq t_{i+1}$

B-splines are formed by joining several Bézier curves end on end. Using B-spline is a more effective method because, for Bézier curves, the number of control points is directly related to the degree of the curve. As done in Bézier representation, a curve can also be represented with an affine combination of some control points as

$$C(t) = \sum p_i N_i^n(t) \tag{3.19}$$

Where N are called basis spline functions which can be calculated with the degree.

B-Splines can be defined with shape functions and vertices set. To define b-splines with $m + 1$ knots, we must divide the target cluster into m intervals. t represents any point in the target cluster, and t_i, where i is between 0 and m, represents the location of knots. The term p represents the degree of shape functions. When $p = 0$ splines do not have continuity(1), 0^{th} order has the purpose of calculating higher orders instead of generating a spline.

$$N_{i,0}(t) = \begin{cases} 1 & if \quad t_i \leq t < t_{i+1} \\ 0 & otherwise \end{cases} \tag{3.20}$$

Beginning from 0^{th} order, remaining ordered basis functions($N_{i,p}$) are calculated with the one before ($N_{i,p-1}$) (2). For all the t values, the sum of $N_{i,p}(t_n)$ must be equal to 1.

$$N_{i,p}(t) = \frac{t-t_i}{t_{i+p}-t_i} N_{i,p-1}(t) + \frac{t_{i+p+1}-t}{t_{i+p+1}-t_{i+1}} N_{i+1,p-1}(t) \tag{3.21}$$

After the desired function gets, only the missing part becomes vertices, where P_i is the set of vertices. The resultant curve can be defiAfter the desired function gets, only the missing part becomes vertices, where P_i is the set of vertices. The resultant curve can be defined as the production of vertices and shape functions.

In Figure 3.3, the region which the dashed red line indicates shows which shape functions are used in which degree to calculate the B-Spline in the interval $[t_4, t_5)$ as an example. For the first order, N_4^1 would be enough, and for the second order B-spline projection, N_3^2 and N_4^2 are needed.

To compute $N_{i,1}(t)$, $N_{i,0}(t)$ and $N_{i+1,0}(t)$ are required. Therefore, we can compute $N_{0,1}(t)$, $N_{1,1}(t)$, $N_{2,1}(t)$, $N_{3,1}(t)$ and so on. These $N_{i,1}(t)$'s are written in the third column. Once all $N_{i,1}(t)$'s have been computed, we can compute $N_{i,2}(t)$'s and put them in the fourth column. This process continues until all required $N_{i,p}(t)$'s are computed.

3.4 MATLAB Solution for B-Spline

MATLAB function that can generate shape functions in certain intervals has generated extremely parametric functions to make it more flexible and easy to use. There are only four inputs we need to insert;

- nok(integer): Number of knots
- xin(array): Solution domain ($x - axis$)
- order(integer): Order of shape function
- plotcheck(logical): true(generates plots for shape functions to check them)

After defining some fundamental parameters, $noel$ is assigned as 50. This value generates equally spaced virtual data locations between control points. The purpose of this parameter is to increase the smoothness of shape functions when the amount of data set is relatively low. After generating new x values, equally spaced control point locations are collected. This location set starts with the smallest value in the data set and ends with the greatest value. Other locations are generating uniformly spaced inside of those points. $knot\_loc$ represents indices of knot location values,

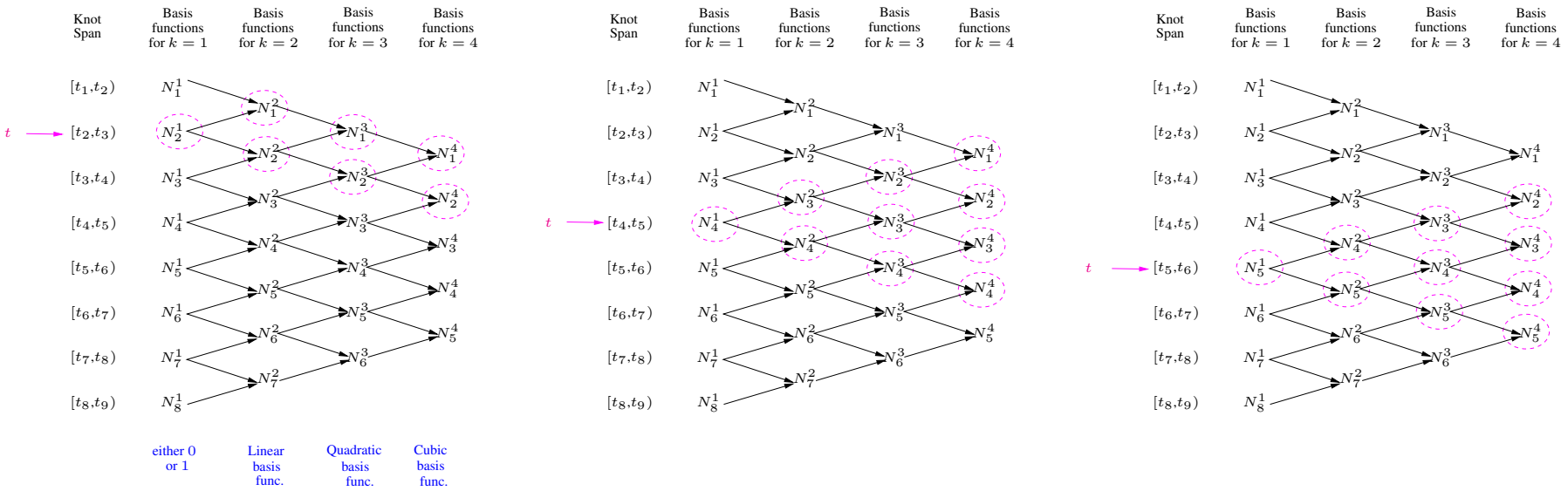

Figure 3.3: Triangular algorithm for calculation of knot span in the desired degree

and $knot\_xin$ represents knot values. Note that, until this point, only the first and last elements of the data set have been used.

As described in Figure 3.3 to not lose the continuity of the basis vectors, some control points should be added to the right and left-hand sides. The number of control points that should be added depends on the order of the shape function that the input asks. So that the input set should be extended on both sides, and new control point locations should be defined. After this definition, the database entered as input was appending the virtual set and sorted again to get precise results. A unique function is used to eliminate any duplication. Since $knot\_loc$ values have shifted, they need to be updated with new values by using the search function, and this process also helps to obtain added control points and their locations.

After perfect assignation of control points and all x values, shape functions can be calculated using equations 3.20 and 3.21. With the help of very successful array management of MATLAB and de Boor's algorithm [38], the computational time is significantly decreasing.

The final part of the code aims to extract only the needed part of the shape function so that the extra knots and x values added to the left and right sides are extracted in the final section. This process aims to keep consistency between input and output so that the equation can be solved smoothly. The plot section is activated when $plotcheck$ is assigned as 'true'.

Figure 3.4a shows the shape functions of the first degree within the desired interval. This figure shows the initial point of the basis function calculation and is an excellent example of equation 3.20. For this degree, it is hard to obtain a meaningful curve, so the 0^{th} order can be considered as the initialization part of the B-Splines basis functions. After this point, equation 3.21 reads and calculates the rest of the shape functions. Dashed lines represent control point locations, and in every interval, the number of curves with nonzero values should equal the degree of the basis function set.

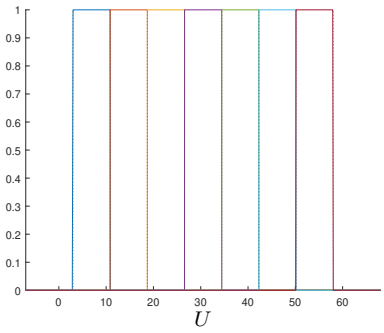

(a) Basis functions of 1^{st} degree

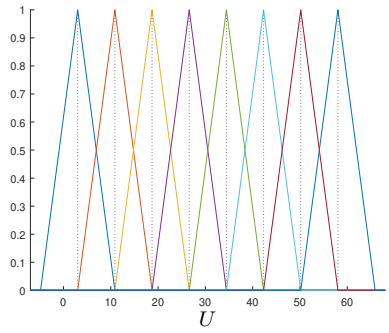

(b) Basis functions of 2^{nd} degree

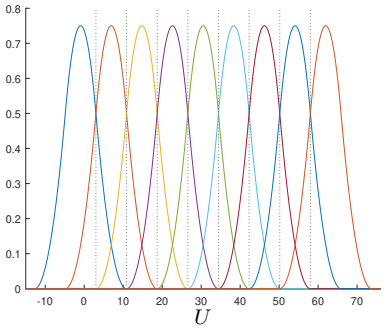

(c) Basis functions of 3^{rd} Degree

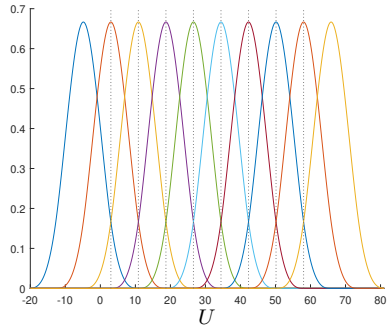

(d) Basis functions of 4^{th} Degree

Figure 3.4: Uniform basis functions for different degrees.

With the help of MATLAB code for basis vector generation, as seen in Figure 3.4, shape functions have been plotted for the desired order. Basis vector code is designed to obtain the basis function with any degree and number of control points. All of the results can be used to plot any B-Spline, but Figure 3.4a is first degree and not practical to get a continuous spline curve, so in all plots, a minimum second degree used. The accuracy of the curve for fitting increases with the degree also, so there is a need for optimization to get satisfactory results with the lowest degree for the computation time reduction.

In Figure 3.5, the transition from basis vector to B-Spline has shown. With the help of equation 3.19, B-Splines are generated with the product of vertice set and basis vectors; the basis vector's degree determines the B-Spline curve's degree. While the degree increases, the computational cost increases; on the other hand, the curve's smoothness also increases. The example of smoothness can be seen in Figure 3.5a;

with the second degree of basis functions, the curve generated became continuous but linear. We can generalize this by saying that the n^{th} order of basis functions can create curves that have continuity up to its $(n-1)^{th}$ derivative. We can also see that if we increase the degree, the number of basis functions and control points that affect the spline segment between control points also increases.

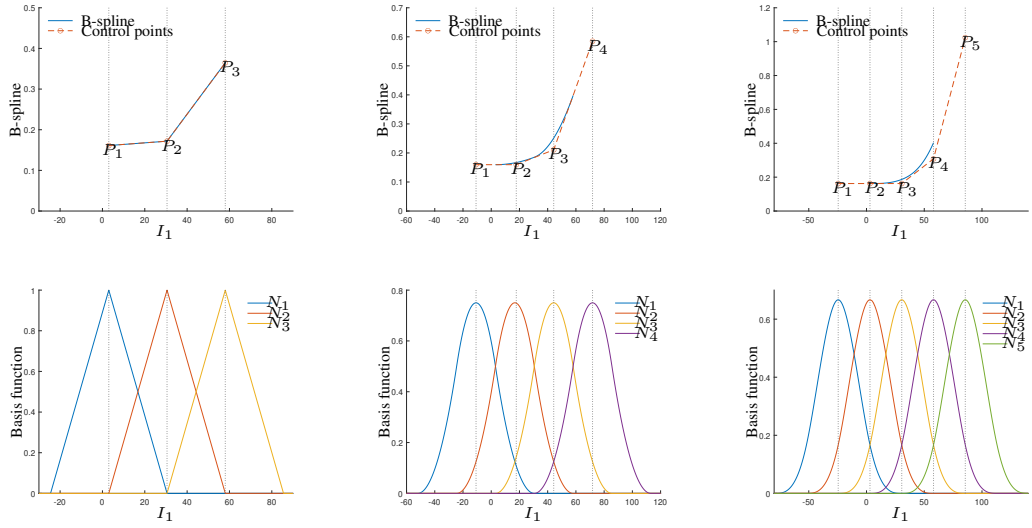

(a) Shape functions N_i for equally spaced 5 knots and 3 control points

(b) Shape (basis) functions N_i for equally spaced 7 knots and 4 control points

(c) Shape functions N_i for equally spaced 9 knots and 5 control points

Figure 3.5: Shape functions and resultant B-Spline examples

CHAPTER 4

DATA-DRIVEN MODELING OF HYPERELASTIC MATERIALS

The data-driven approach for material modeling will be discussed and explained in this chapter. The four different kinematic models studied in this thesis are listed below;

- invariant based model
- modified invariant based model
- principal stretch based model
- modified principal stretch based model.

4.1 Introduction

The mechanical behavior of rubberlike materials due to their highly nonlinear behavior and high level of deformation strains are modeled as hyperelastic. It is not easy to define one general potential function which works for all types of hyperelastic materials. Data-driven material modeling aims to define a general data-driven model for all types of hyperelastic materials by fitting the partial derivatives of the potential function used in stress definitions to experimental stress-strain data. Another aim here is to imitate material behavior without losing any data. The use of spline generation and optimization solvers are facts that make it easy to build a data-driven model.

4.2 Treloar's Data

Treloar's experimental rubber data is commonly used to validate models for rubberlike materials. The data represents rubber at 20^oC within a substance of 8% of sulfur.

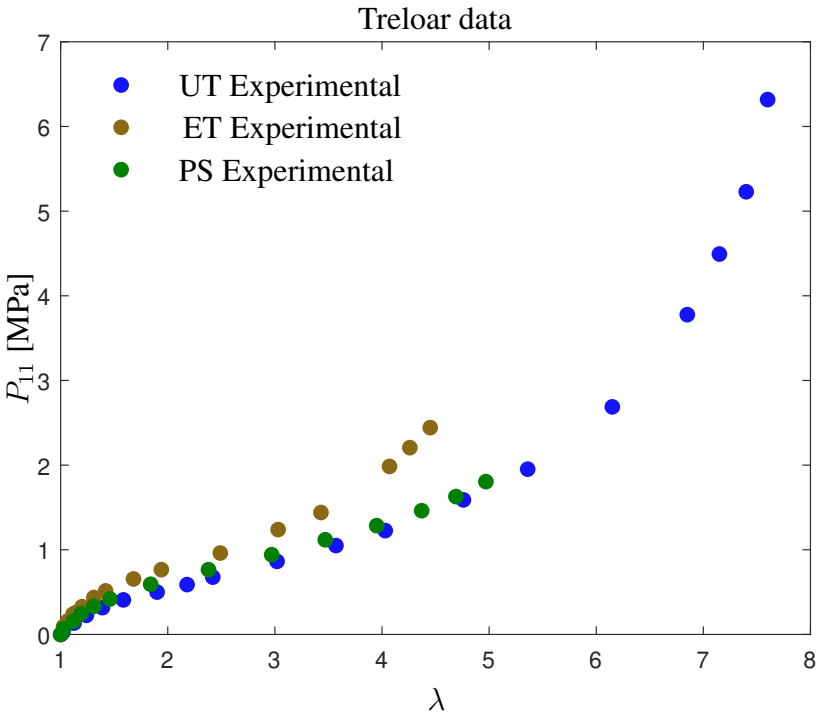

Figure 4.1: Treloar data

Treloar data in Figure 4.1 is taken from experiments conducted with natural rubber by Professor Leslie Ronald George Treloar [12]. Data consists of uniaxial tension data within the stretch range of up to 7.6, equibiaxial tension data within the range of up to 4.97, and pure shear up to 4.45.

4.3 Constraints

We apply simple restriction rules between control points to achieve physically consistent results. The stability or convexity of the model is achieved by the positive first derivative relationship between sequential control points, or simply by forcing the control points to be larger than the previous control point. Approximate second and third order derivatives are also derived using the finite difference of the control points as shown in equation 4.2. Limiting the second and third derivatives or their numerator as given in 4.1, if necessary, can be beneficial for the smoothness of the

solution.

$$
\begin{aligned}
&constraint_1 \rightarrow k_{i+1} - k_i > t_1 \\
&constraint_2 \rightarrow k_{i+2} - k_{i+1} + k_i > t_2 \\
&constraint_3 \rightarrow k_{i+3} - 3k_{i+2} + 3k_{i+1} - k_i > t_3
\end{aligned} \tag{4.1}
$$

In Amores' [10] [11] the employed equations for the stability and smoothness are given in equation 4.2

$$
\begin{aligned}
D_j^{(1)} &= \frac{P_{j+1} - P_j}{h} \\
D_j^{(2)} &= \frac{P_{j+2} - 2P_{j+1} + P_j}{h^2} \\
D_j^{(3)} &= \frac{P_{j+3} - 3P_{j+2} + 3P_{j+1} - P_j}{h^3}
\end{aligned} \tag{4.2}
$$

where h is the knot span or segment size of the B-spline. Here example of D matrices for a data-driven model with two sets of 5 vertices is given. Even though there are two sets of vertices for each partial derivative term of the model each constraint can be written in a single matrix for all the vertices.

$$
D_j^{(1)} = \frac{1}{h}\begin{bmatrix}
-1 & 1 & 0 & 0 & 0 & 0 & 0 & 0 & 0 & 0 \\
0 & -1 & 1 & 0 & 0 & 0 & 0 & 0 & 0 & 0 \\
0 & 0 & -1 & 1 & 0 & 0 & 0 & 0 & 0 & 0 \\
0 & 0 & 0 & -1 & 1 & 0 & 0 & 0 & 0 & 0 \\
0 & 0 & 0 & 0 & 0 & -1 & 1 & 0 & 0 & 0 \\
0 & 0 & 0 & 0 & 0 & 0 & -1 & 1 & 0 & 0 \\
0 & 0 & 0 & 0 & 0 & 0 & 0 & -1 & 1 & 0 \\
0 & 0 & 0 & 0 & 0 & 0 & 0 & 0 & -1 & 1
\end{bmatrix} \tag{4.3}
$$

$$
D_j^{(2)} = \frac{1}{h^2}\begin{bmatrix}
1 & -2 & 1 & 0 & 0 & 0 & 0 & 0 & 0 & 0 \\
0 & 1 & -2 & 1 & 0 & 0 & 0 & 0 & 0 & 0 \\
0 & 0 & 1 & -2 & 1 & 0 & 0 & 0 & 0 & 0 \\
0 & 0 & 0 & 0 & 0 & 1 & -2 & 1 & 0 & 0 \\
0 & 0 & 0 & 0 & 0 & 0 & 1 & -2 & 1 & 0 \\
0 & 0 & 0 & 0 & 0 & 0 & 0 & 1 & -2 & 1
\end{bmatrix} \tag{4.4}
$$

$$
D_j^{(3)} = \frac{1}{h^3}\begin{bmatrix}
-1 & 3 & -3 & 1 & 0 & 0 & 0 & 0 & 0 & 0 \\
0 & -1 & 3 & -3 & 1 & 0 & 0 & 0 & 0 & 0 \\
0 & 0 & 0 & 0 & 0 & -1 & 3 & -3 & 1 & 0 \\
0 & 0 & 0 & 0 & 0 & 0 & -1 & 3 & -3 & 1
\end{bmatrix} \tag{4.5}
$$

Since the need is inequality about them and increasing the effect of constraints may lower the Quality of Fit, the first and second constraints only need to be positive so that the term h vanishes for the first and second Invariant.

4.4 Error Calculation

There are more than 40 hyperelastic models for rubberlike materials in the literature, and some fit well where stretch levels are really low, some fit well only for the Gaussian region, and some work well in the non-Gaussian region shown in Figure 4.2. To evaluate the performance of hyperelastic models, Dal [39] proposes the 4.6 equation, called quality of fit.

$$\chi^2 = \frac{(P_{11}(\lambda_i) - P_{11,exp}(\lambda_i))^2}{P_{11,exp}(\lambda_i)} \tag{4.6}$$

Here, the same formula is used to compare the performance of the proposed data-driven models for all regions.

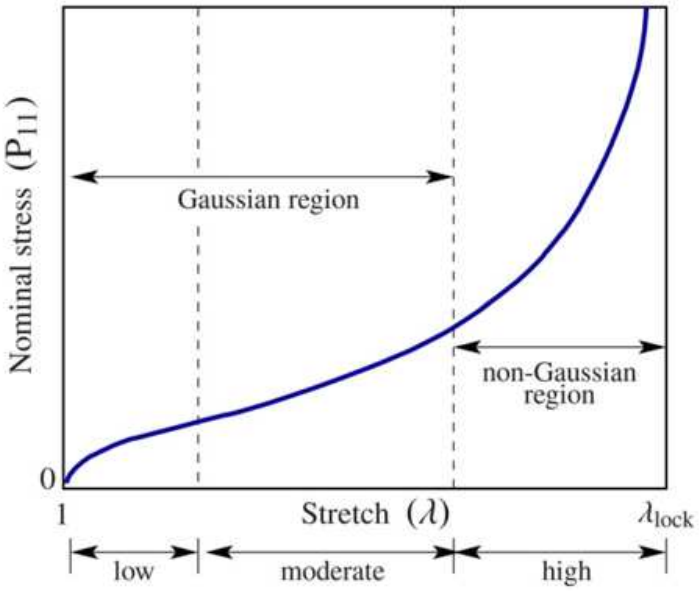

Figure 4.2: Regions of stretch data (Retrieved from [39])

In the below tables which show errors, region 1 corresponds low range, region 2 corresponds low and mid-range, and region 3 corresponds complete range of the data which are shown in Figure 4.2.

4.5 Invariant Based Data-Driven Model

In this model, without giving any definition for the free energy function, $\psi = \bar{\psi}(I_1, I_2, I_3)$ is assumed to be in invariant basis form and the Lagrangian and Euler stresses are defined by the application of the chain rule. Since it is assumed to be no volume change during deformation only the partial derivatives with respect to I_1 and I_2 are replaced with B-spline definitions.

4.5.1 Methodology

First of all the stretches and the stresses under homogenous deformations are given for uniaxial tension, equibiaxial tension, and pure shear. Experiments are usually done with the displacement-based setup, and cross-sectional area changes are not taken into account, the stretches and nominal stresses obtained from these tests are the experimental inputs of the data-driven model.

$$\mathbf{F} = \begin{bmatrix} \lambda & 0 & 0 \\ 0 & \frac{1}{\sqrt{\lambda}} & 0 \\ 0 & 0 & \frac{1}{\sqrt{\lambda}} \end{bmatrix} \text{ and } \mathbf{P} = \begin{bmatrix} P_1 & 0 & 0 \\ 0 & 0 & 0 \\ 0 & 0 & 0 \end{bmatrix} \tag{4.7}$$

for equibiaxial tension;

$$\mathbf{F} = \begin{bmatrix} \lambda & 0 & 0 \\ 0 & \lambda & 0 \\ 0 & 0 & \frac{1}{\lambda^2} \end{bmatrix} \text{ and } \mathbf{P} = \begin{bmatrix} P_1 & 0 & 0 \\ 0 & P_1 & 0 \\ 0 & 0 & 0 \end{bmatrix} \tag{4.8}$$

for pure shear;

$$\mathbf{F} = \begin{bmatrix} \lambda & 0 & 0 \\ 0 & 1 & 0 \\ 0 & 0 & \frac{1}{\lambda} \end{bmatrix} \text{ and } \mathbf{P} = \begin{bmatrix} P_1 & 0 & 0 \\ 0 & P_2 & 0 \\ 0 & 0 & 0 \end{bmatrix} \tag{4.9}$$

This can lead us to the left Cauchy-Green deformation tensor with relation;

$$\mathbf{B} = \mathbf{F}\mathbf{F}^T \tag{4.10}$$

And with the left Cauchy-Green deformation tensor we can calculate the invariants as;

$$
\begin{aligned}
I_1 &:= tr(\mathbf{B}) = B_{ii} = \lambda_1^2 + \lambda_2^2 + \lambda_3^2 \\
I_2 &:= \frac{1}{2}[(tr\mathbf{B})^2 - tr(\mathbf{B}^2)] = \frac{1}{2}(B_{ii}^2 - B_{jk}B_{kj}) = \lambda_1^2\lambda_2^2 + \lambda_2^2\lambda_3^2 + \lambda_3^2\lambda_1^2 \\
I_3 &:= det\mathbf{B} = J^2 = \lambda_1^2\lambda_2^2\lambda_3^2
\end{aligned}
\tag{4.11}
$$

The Eulerian stress is defined by the application of the chain rule is given as:

$$
\boldsymbol{\tau} = 2\partial_{\boldsymbol{g}}\psi = 2\left[\frac{\partial\psi}{\partial I_1}\frac{\partial I_1}{\partial \boldsymbol{g}} + \frac{\partial\psi}{\partial I_2}\frac{\partial I_2}{\partial \boldsymbol{g}} + \frac{\partial\psi}{\partial J}\frac{\partial J}{\partial \boldsymbol{g}}\right] \tag{4.12}
$$

$\boldsymbol{\tau}$ is the Kirchhoff stress. Substituting the derivatives with respect to spatial metric $\boldsymbol{g}$, given in detail in [39], and rearranging the equation gives

$$
\boxed{\boldsymbol{\tau} = 2(c_1 + I_1 c_2)\,\boldsymbol{b} - 2c_2\boldsymbol{b}^2 - p\boldsymbol{g}^{-1}} \tag{4.13}
$$

$$
\text{with} \quad c_1 = \frac{\partial\psi}{\partial I_1} \quad c_2 = \frac{\partial\psi}{\partial I_2} \quad p = -J\partial_J\psi \tag{4.14}
$$

In the equation 4.13, I_1, I_2, and λ_i are already known from stretch values in the experimental data. c_1 and c_2 will be replaced with the B-spline definitions given in equation 4.15.

$$
c_1 = N_1 p_1 \quad \text{and} \quad c_2 = N_2 p_2 \tag{4.15}
$$

N_1 and N_2 are the basis functions, p_1 and p_2 are representing their vertice sets respectively. So equation leads

$$
\tau_i = 2(N_1(\lambda_i)p_1 + I_1(\lambda_i)N_2(\lambda_i)p_2)\lambda_i^2 - 2N_2(\lambda_i)p_2\lambda_i^4 - p \tag{4.16}
$$

with at a given λ_i calculated I_1 and I_2

$$
N_1 p_1 = [N_1(I_1) \quad \cdots \quad N_n(I_1)] \begin{pmatrix} \hat{P}_{I_{1_1}} \\ \vdots \\ \hat{P}_{I_{1_n}} \end{pmatrix}
$$

$$c_2 = [N_1(I_2) \quad \cdots \quad N_m(I_2)] \begin{pmatrix} \hat{P}_{I_{21}} \\ \vdots \\ \hat{P}_{I_{2m}} \end{pmatrix}$$

where n, m are the number of B-spline control points with prescribed x values I_{11}, $\cdots$, I_{1n} and I_{21}, $\cdots$, I_{2m} whose limits are determined from the available ranges in the tests.

The transition from Kirchhoff stress to the first Piola-Kirchhoff stress (nominal stress) can be calculated as

$$\boldsymbol{P} = \boldsymbol{\tau}\boldsymbol{F}^{-1} \tag{4.17}$$

We can derive an error relation from the above relation and observe the final relation to solving.

$$E = \frac{1}{n_{data}} \sum (P - P_{exp})^2 \tag{4.18}$$

To get final stress values, the only thing we should do to solve the E equation for the p_1 set and p_2 set is to minimize the error. This can be done in many ways, but this problem is solved with Nonlinear Optimization tools in this thesis. On the other hand, since this is an optimization problem, there should be some constraints to get a physically consistent model.

4.5.2 Results for Invariant Based Approach

The Treloar and Kawabata datasets are used to validate and evaluate the performance of the proposed model.

4.5.2.1 Simultaneous Fit Result to Treloar Data

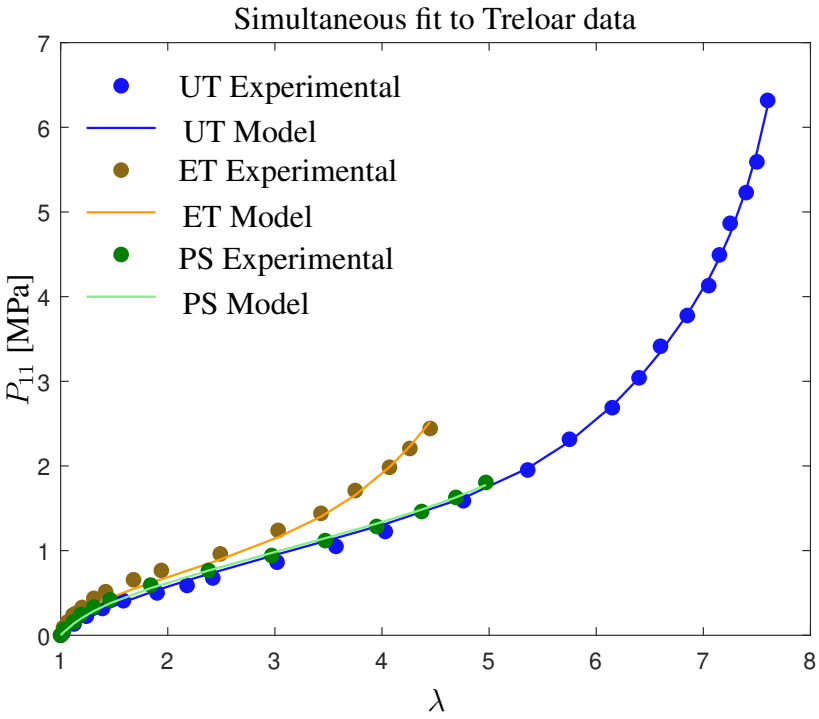

Figure 4.3: Invariant based approach: Treloar data

The invariant based model is fit to Treloar data simultaneously as shown in Figure 4.3. In this fit, all experiments are simultaneously included in the optimization problem; also weights of all data are included in this optimization problem. Values of the weight distribution can be seen in Table 4.2.

Table 4.1: Invariant based approach: Vertices fitted to Treloar data

	c_1	c_2
p_1	0.162854	0.002655
p_2	0.163004	0.002752
p_3	0.163019	0.002758
p_4	0.163047	0.002759
p_5	0.207318	0.002760
p_6	0.298758	0.002760
p_7	0.428004	0.002762
p_8	1.681677	0.002781

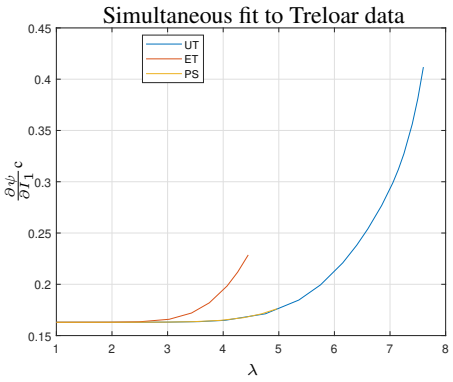

(a) $\frac{\partial \psi}{\partial I_1}$ vs. λ graph for invariant based model

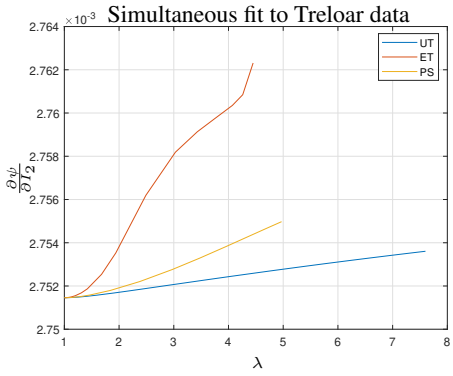

(b) $\frac{\partial \psi}{\partial I_2}$ vs. λ graph for invariant based model

Figure 4.4: Derivatives of energy function with respect to invariants

In Table 4.1, vertice values calculated through optimization have been shown. The optimized values also obey the stability constraint rules given in equation 4.2. The invariant based derivative values c_1 and c_2, calculated with optimized vertice set and basis function, have been plotted in Figure 4.4a and Figure 4.4b respectively. Derivatives must be greater than zero because of the model stability requirement. Figure 4.4a and Figure 4.4b show that the proposed model satisfies this requirement.

Table 4.2: Invariant based approach: Weights fitted to Treloar data

	w_{ut}	w_{et}	w_{ps}
weights	0.20	0.20	0.60

Table 4.3: Invariant based approach: QOF values for Treloar data

	Region 1	Region 2	Region 3
UT	0.0211	0.0525	0.0631
ET	0.0577	0.1393	0.1502
PS	0.0312	0.0375	0.0409
ALL	0.1101	0.2294	0.2543

The quality of fits for all regions is shown in Table 4.3 for all three experiments, and

the cumulative results of all experiments are also shown. Although the fit qualities are quite good for all regions, the best fit is obtained in Region 1 due to the different trends of equibiaxial and uniaxial tension tests in medium and high-strain regions.

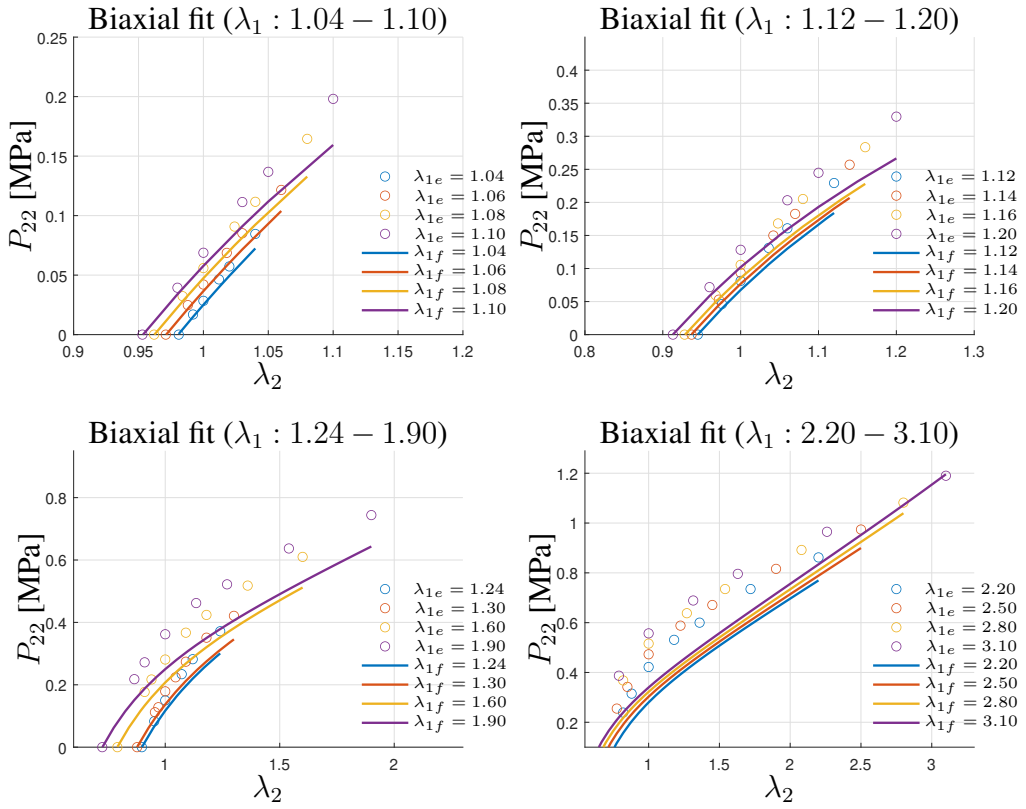

Figure 4.5: Invariant based model predictions for Kawabata data from data points obtained from Treloar data

In Figure 4.5, the same simultaneous fitted vertice set is used to plot Kawabata experiment data for biaxial tension to see the model's performance within similar but not exact physical conditions.

4.5.2.2 Biaxial Fits to Kawabata Data

Validation is important for proposed models and their application methods, here the same method is applied to the Kawabata data set. All fits are done with the same number of control points and degrees with the Treloar data fits to compare the performance easily. Fitted results can be seen in Figure 4.6.

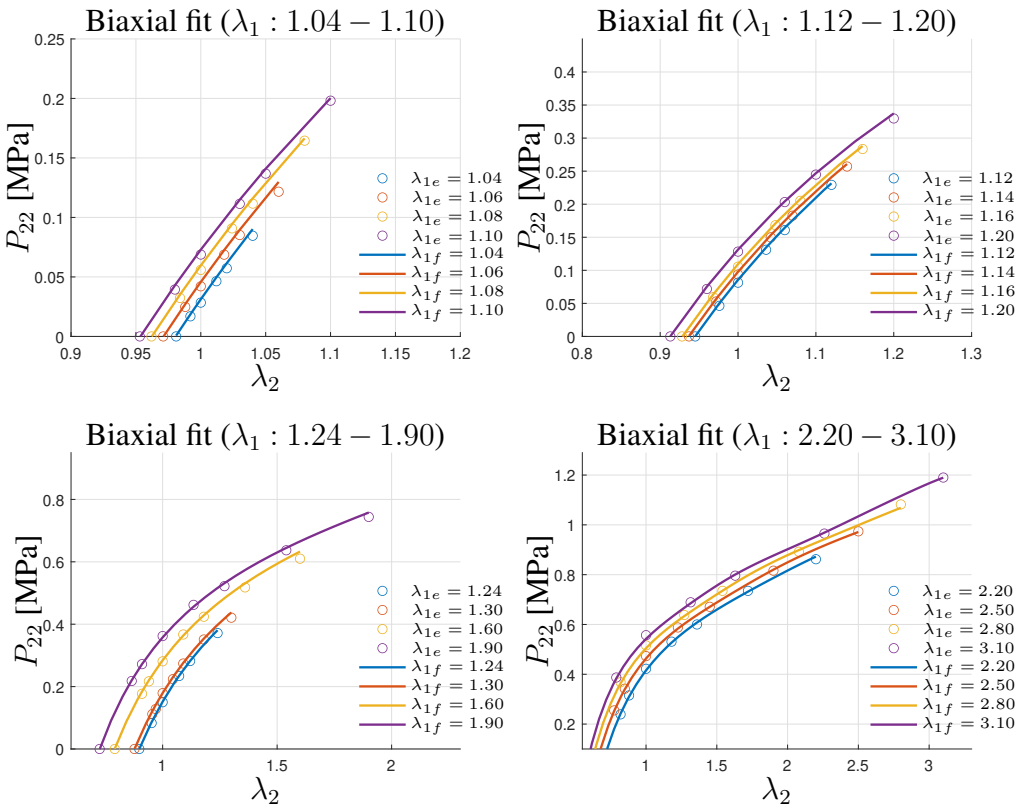

Figure 4.6: Invariant based model predictions for Kawabata data

Table 4.4: Invariant based approach: Vertices fitted to Kawabata data

	c_1	c_2
p_1	0.318096	0.093595
p_2	0.154592	0.014285
p_3	0.142211	0.010597
p_4	0.131771	0.007458
p_5	0.128147	0.007288
p_6	0.114500	0.005725

The proposed model gives quite nice fits for all Kawabata tests in different stretch levels. The vertice sets of the Kawabata fit are given in Table 4.4. These vertices were also tried for Treloar data fits just to see their performance for higher stretch levels. Since the stretch range of Kawabata data is much smaller than that of Treloar data, model success is not good for stretch values greater than 3, see Figure 4.7.

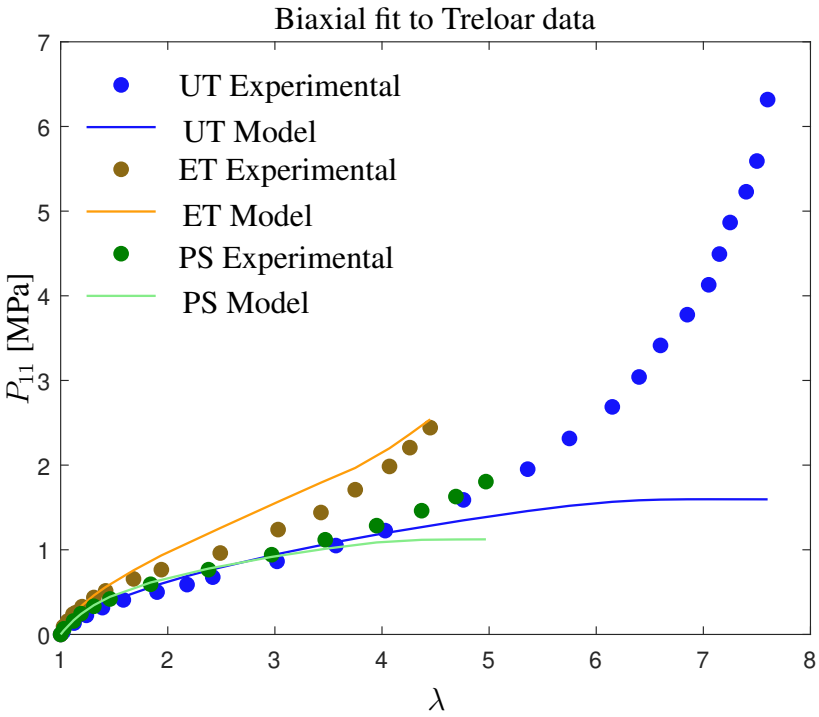

Figure 4.7: Invariant based model predictions for Treloar data with vertice points obtained from Kawabata data

4.6 Modified Invariant Based Data-Driven Model

As an alternative to the direct use of the first two invariants, here the B-spline interpolation is employed for two macro-kinematic variables which are functions of the first and second invariants.

4.6.1 Methodology

The methodology is pretty similar to the invariant based approach. The only difference is, instead of I_1 and I_2, the model uses two other macro kinematic variables, namely the longitudinal stretch λ_{ch} and the areal stretch ν_{ch}, which are defined by reference to [35]. The longitudinal stretch λ_{ch} and the areal stretch ν_{ch} are related to I_1 and I_2 and they are defined as;

$$\lambda_{ch} = \sqrt{\frac{I_1}{3}} \quad \text{and} \quad \nu_{ch} = \sqrt[3]{\frac{I_2}{3}} \quad . \tag{4.19}$$

B-spline interpolation is employed for the partial derivatives of free energy function

with respect to these macro-kinematic variables. Thus, the derivatives of the free energy function with respect to the invariants are given as;

$$c_1 = \frac{\partial \psi}{\partial I_1} = \frac{\partial \psi}{\partial \lambda_{\text{chn}}} \frac{\partial \lambda_{\text{chn}}}{\partial I_1} \tag{4.20}$$

$$c_2 = \frac{\partial \psi}{\partial I_2} = \frac{\partial \psi}{\partial \nu_{\text{chn}}} \frac{\partial \nu_{\text{chn}}}{\partial I_2} \tag{4.21}$$

where

$$\frac{\partial \lambda_{\text{chn}}}{\partial I_1} = \frac{1}{6} \frac{1}{\lambda_{\text{chn}}^2} \quad , \quad \frac{\partial \nu_{\text{chn}}}{\partial I_2} = \frac{1}{9} \frac{1}{\nu_{\text{chn}}^2} \quad . \tag{4.22}$$

Finally, the derivatives of the free energy function with respect to λ_{chn} and ν_{chn} are estimated by B-spline interpolations.

$$\hat{c}_1 = \frac{\partial \psi}{\partial \lambda_{\text{chn}}} = [N_1(\lambda_{\text{chn}}) \quad \cdots \quad N_n(\lambda_{\text{chn}})] \begin{pmatrix} \hat{P}_{\lambda_{\text{chn}\,1}} \\ \vdots \\ \hat{P}_{\lambda_{\text{chn}\,n}} \end{pmatrix}$$

$$\hat{c}_2 = \frac{\partial \psi}{\partial \nu_{\text{chn}}} = [N_1(\nu_{\text{chn}}) \quad \cdots \quad N_n(\nu_{\text{chn}})] \begin{pmatrix} \hat{P}_{\nu_{\text{chn}\,1}} \\ \vdots \\ \hat{P}_{\nu_{\text{chn}\,n}} \end{pmatrix}$$

The rest of the calculations are the same as the invariant based model.

4.6.2 Results for Modified Invariant Based Approach

The performance of the proposed modified invariant based approach is assessed by fits to Treloar and Kawabata data sets.

4.6.2.1 Treloar Based Simultaneous Fit Results

The modified invariant based model is used to fit Treloar data simultaneously as shown in Figure 4.8. In this fit, all experiments are simultaneously included in the optimization problem; also weights of all data are included in this optimization problem. Values of the weight distribution can be seen in Table 4.6.

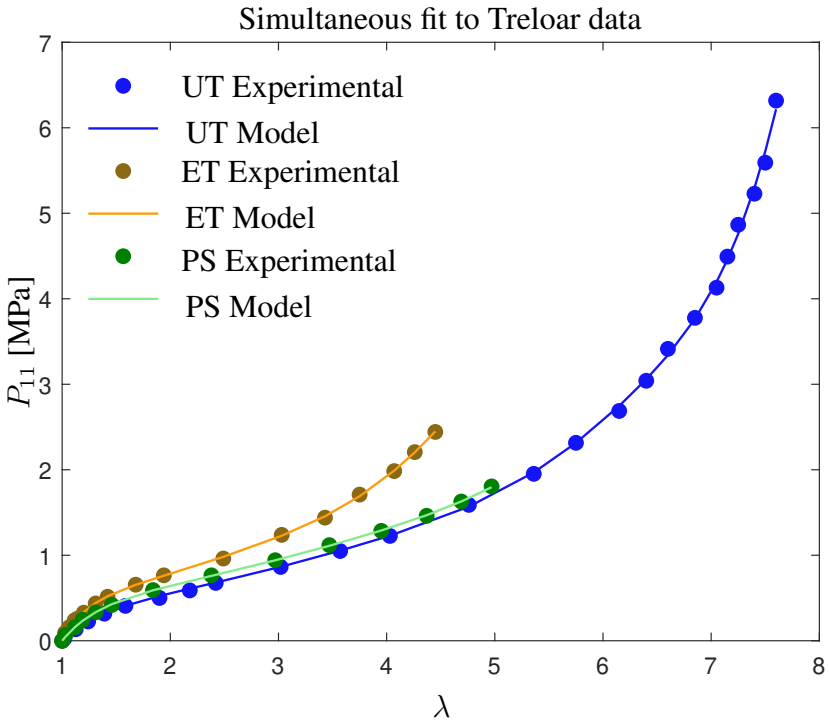

Figure 4.8: Modified invariant based approach: Treloar data

Table 4.5: Modified invariant based approach: Vertices fitted to Treloar data

	$\hat{c}_1$	$\hat{c}_2$
p_1	0.479793	0.200090
p_2	0.727134	0.396911
p_3	1.064566	0.426831
p_4	1.980226	0.443884
p_5	2.979472	0.487106
p_6	6.055671	0.519046
p_7	10.76522	0.544376
p_8	70.22761	0.908433

Table 4.5 gives the values of the vertice sets calculated through optimization. The optimized values also obey the stability constraint rules shown in equation set 4.2. The partial derivative values $\hat{c}_1$ and $\hat{c}_2$ with respect to modified invariants, calculated with optimized vertice sets are given in Figure 4.9a and 4.9b. The figures show that

the effect of longitudinal stretches increases as the stretch increases, but the effect of areal stretches decreases.

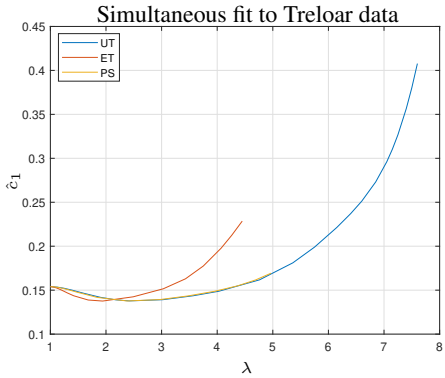

(a) $\hat{c}_1$ vs. λ graph for modified invariant based model

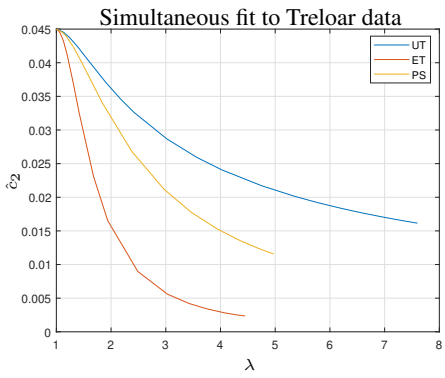

(b) $\hat{c}_2$ vs. λ graph for modified invariant based model

Figure 4.9: Derivatives of energy function with respect to modified invariants

The quality of fits for all regions are shown in Table 4.7 and cumulative results of all experiments are also shown in the same table. Compared to the invariant based approach fits are much better in all regions. This improvement in the fit is thought to be due to a better estimation of the I_2 effect in the modified invariant approach.

Table 4.6: Modified invariant based approach: Weights fitted to Treloar data

	w_{ut}	w_{et}	w_{ps}
weights	0.20	0.20	0.60

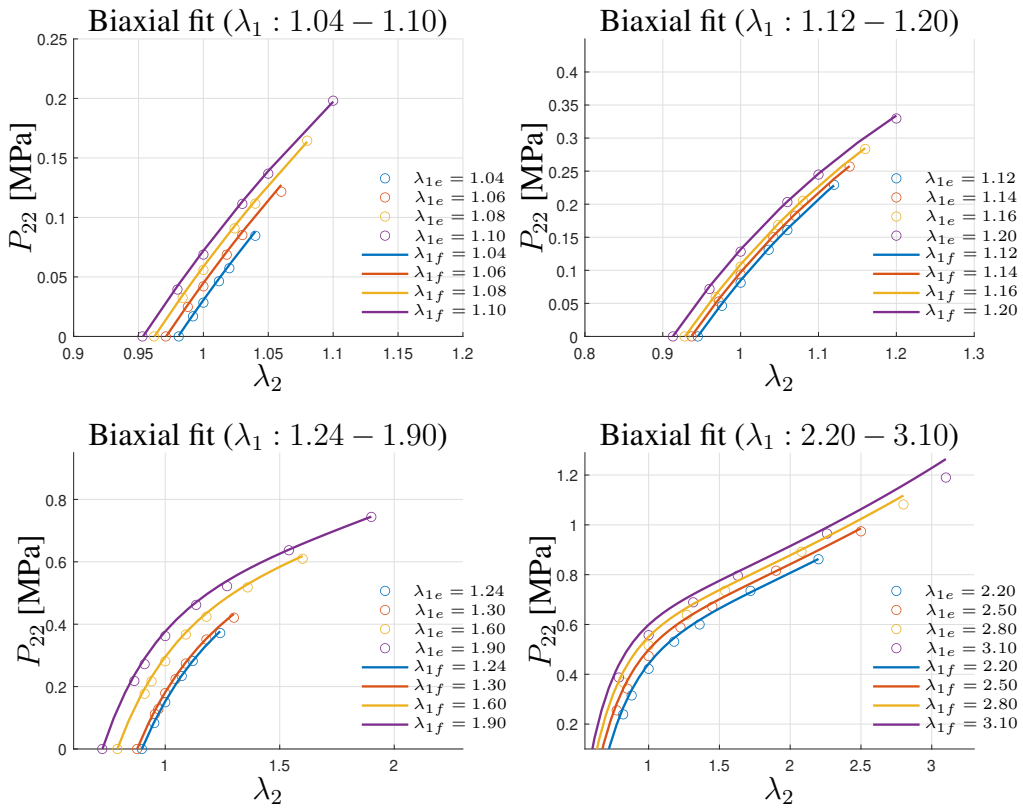

Figure 4.10: Modified invariant based model predictions for Kawabata data from data points obtained from Treloar data

In Figure 4.10, the vertices used in simultaneous fits to Treloar data are employed to estimate the Kawabata data to see the model's performance within similar but not exact physical conditions. The result is much better than the invariant based approach.

Table 4.7: Modified invariant based approach: QOF values for Treloar data

	Region 1	Region 2	Region 3
UT	0.0023	0.0026	0.0151
ET	0.0146	0.0153	0.0158
PS	0.0071	0.0074	0.0076
ALL	0.0242	0.0255	0.0386

4.6.2.2 Kawabata Based Biaxial Fit Results

The modified invariant based model is also validated with Kawabata data. Again all fits are done with the same number of control points and degrees with the Treloar data fits to make it easy to compare. Fitted results can be seen in Figure 4.11 and the vertice sets are given in Table 4.8.

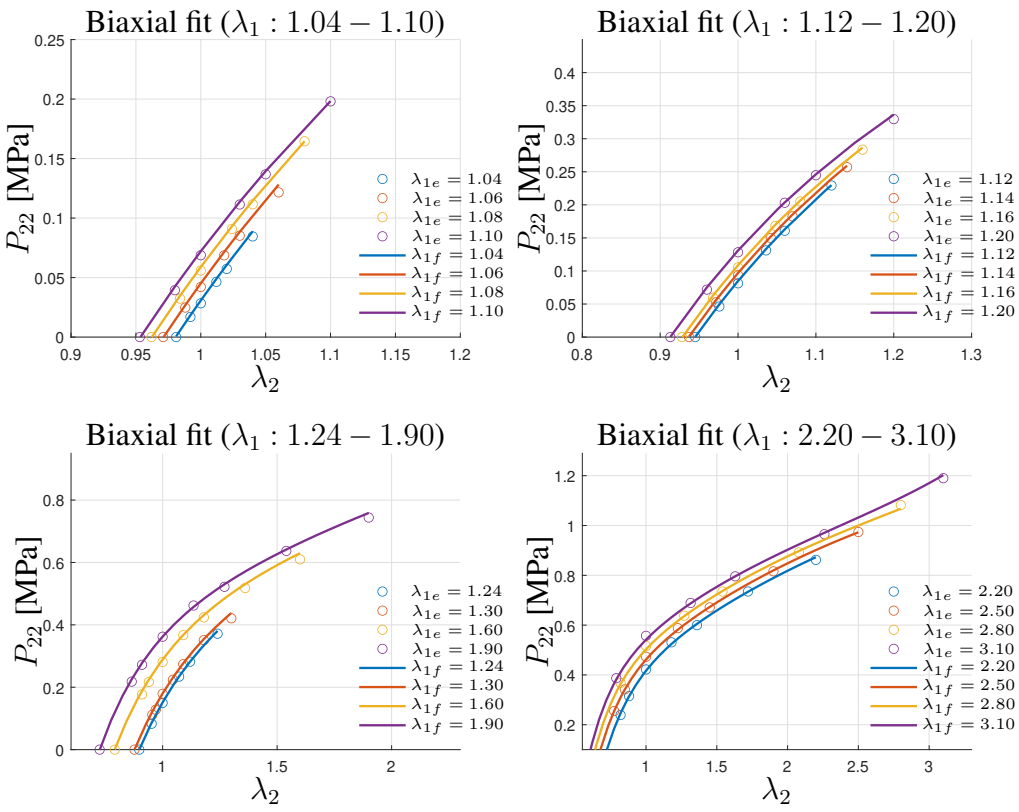

Figure 4.11: Modified invariant based model predictions for Kawabata data

As seen in Figure 4.11 proposed modified invariant model predicts very successfully all Kawabata tests in all stretch levels.

Treloar fit performance is also checked by using the same vertice sets used in Kawabata fits, see Figure 4.12. Since the stretch range of Kawabata data is less than Treloar data, model prediction is not that successful in the non-Gaussian regions.

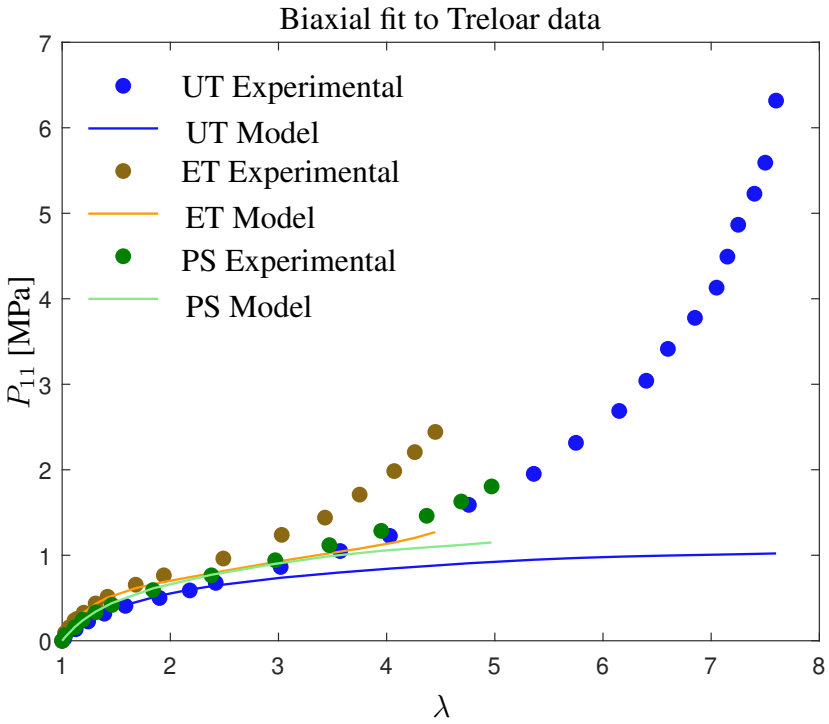

Figure 4.12: Modified invariant based model predictions for Treloar data from vertice points obtained from Kawabata data

Table 4.8: Modified Invariant based approach: Vertices fitted to Kawabata data

	$\hat{c}_1$	$\hat{c}_2$
p_1	0.650509	0.309980
p_2	0.984426	0.327047
p_3	1.329832	0.384145
p_4	1.653477	0.498076
p_5	1.898696	0.575534
p_6	2.321614	0.861077

4.7 Principal Stretch Based Approach

In this section without giving any definition for the free energy function, $\psi = \bar{\psi}(\lambda_1, \lambda_2, \lambda_3)$ is assumed to be in principal stretch basis form and the Lagrangian and Euler stresses are defined by partial derivatives of free energy with respect to principal stretches.

4.7.1 Methodology

The strain energy function is defined as a function of principal stretches $\psi = \tilde{\psi}(\lambda_1, \lambda_2, \lambda_3)$. Stress expressions for the principal stretch based approach are written as;

$$\boxed{\begin{array}{rcccc} \boldsymbol{S} & = & \sum_{a=1}^{3} \frac{1}{\lambda_a} \beta_a \boldsymbol{N}_a \otimes \boldsymbol{N}_a & - & p\boldsymbol{C}^{-1} \\ \boldsymbol{\tau} & = & \sum_{a=1}^{3} \lambda_a \, \beta_a \boldsymbol{n}_a \otimes \boldsymbol{n}_a & - & p\mathbf{1}. \end{array}} \tag{4.23}$$

where $\beta_a = \frac{\partial \psi}{\partial \lambda_a}$ with a=1,2,3 and replaced by B-spline

$$\beta_a = \frac{\partial \psi}{\partial \lambda_a} = \begin{bmatrix} N_1(\lambda_a) & \cdots & N_n(\lambda_a) \end{bmatrix} \begin{pmatrix} \hat{P}_1 \\ \vdots \\ \hat{P}_n \end{pmatrix}$$

4.7.2 Results for Principal Stretch Based Approach

The Treloar and Kawabata datasets are used to validate and evaluate the performance of the proposed model.

4.7.2.1 Treloar Based Simultaneous Fit Results

The simultaneous fit results of the principal stretch based approach to the Treloar data set are given in Figure 4.13. In this fit, all experiments are simultaneously included in the optimization problem; also weights of all data are included in this optimization problem. Values of the weight distribution can be seen in Table 4.10. Since rubber is assumed to be symmetric, there is only one set of vertices that are used for the prediction of the partial derivatives with respect to all principal stretches.

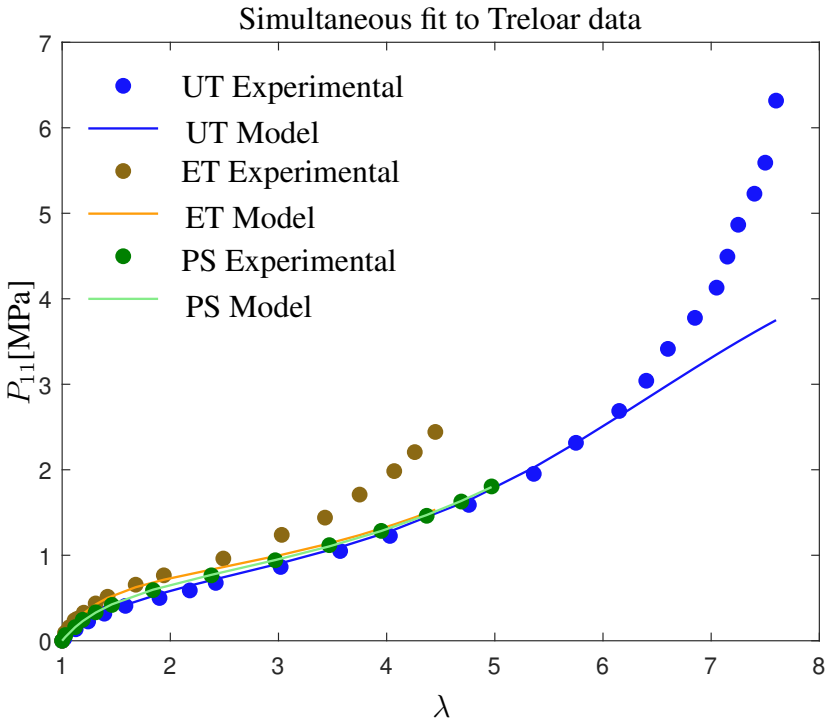

Figure 4.13: Principal stretch based approach: Predictions for the Treloar data

Table 4.9: Principal stretch-based approach: Vertices fitted to Treloar data

p_1	0.108146
p_2	0.108468
p_3	1.371108
p_4	2.540026
p_5	22.53062

Table 4.10: Principal stretch-based approach: Weights fitted to Treloar data

	w_{ut}	w_{et}	w_{ps}
weights	0.20	0.20	0.60

As seen in Figure 4.13 and in Table 4.11 model fits only for the regions of the curve before getting stiffer, for all three test curves. It can be said that the model only works for some parts of the Gaussian region. It has no ability to predict the non-Gaussian

region.

Table 4.11: Principal stretch-based approach: QOF values for Treloar data

	Region 1	Region 2	Region 3
UT	0.7765	5.2585	7.6215
ET	0.0048	0.8222	38.806
PS	0.0016	0.7970	2.8705
ALL	0.7831	6.8777	49.298

In Table 4.9, values calculated through optimization have been shown. The optimized values also obey the stability constraint rules shown in 4.2. In Figure 4.14, the vertices used in simultaneous fits to Treloar data are also employed to estimate the Kawabata data to see the model's performance within similar but not exact physical conditions. Fits are good only for stretch values less than 1.2.

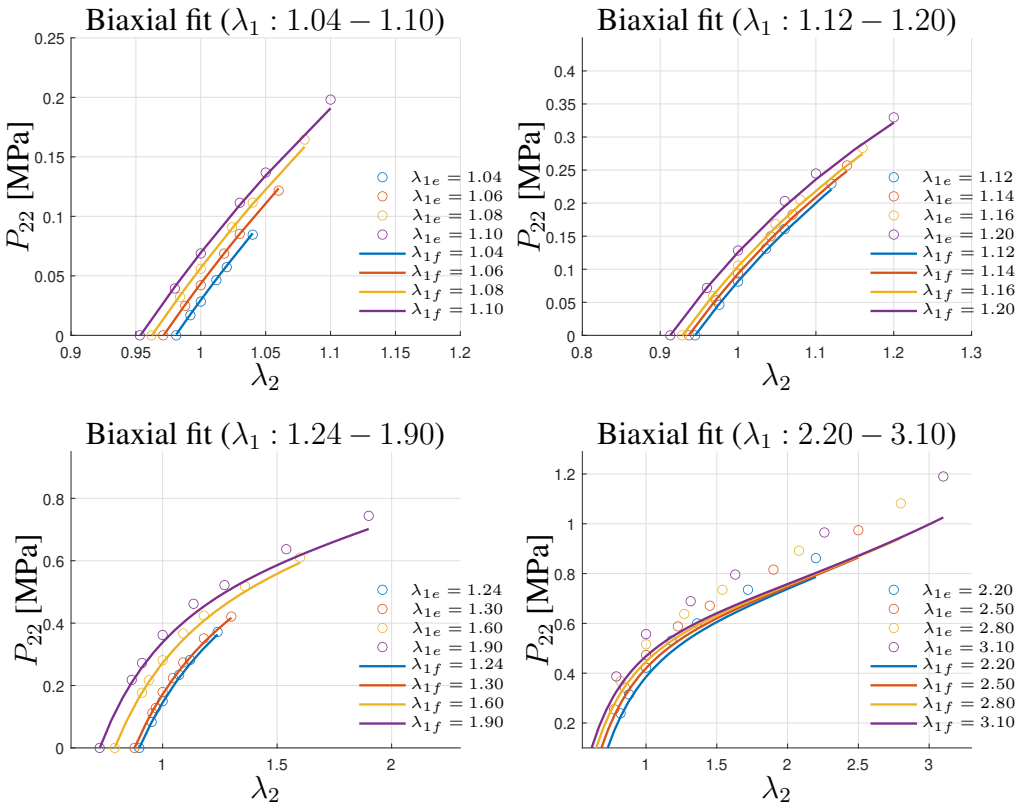

Figure 4.14: Principal stretch based model predictions for Treloar data

4.7.2.2 Kawabata Based Biaxial Fit Results

The performance of the principal stretch based model is evaluated also with Kawabata data. Here the model does not perform well with the same number of vertices used for Treloar data fits, so the vertice number is increased to twelve. Fitted results can be seen in Figure 4.15. Even though the vertice number is increased, the model could not fit well for all the Kawabata tests.

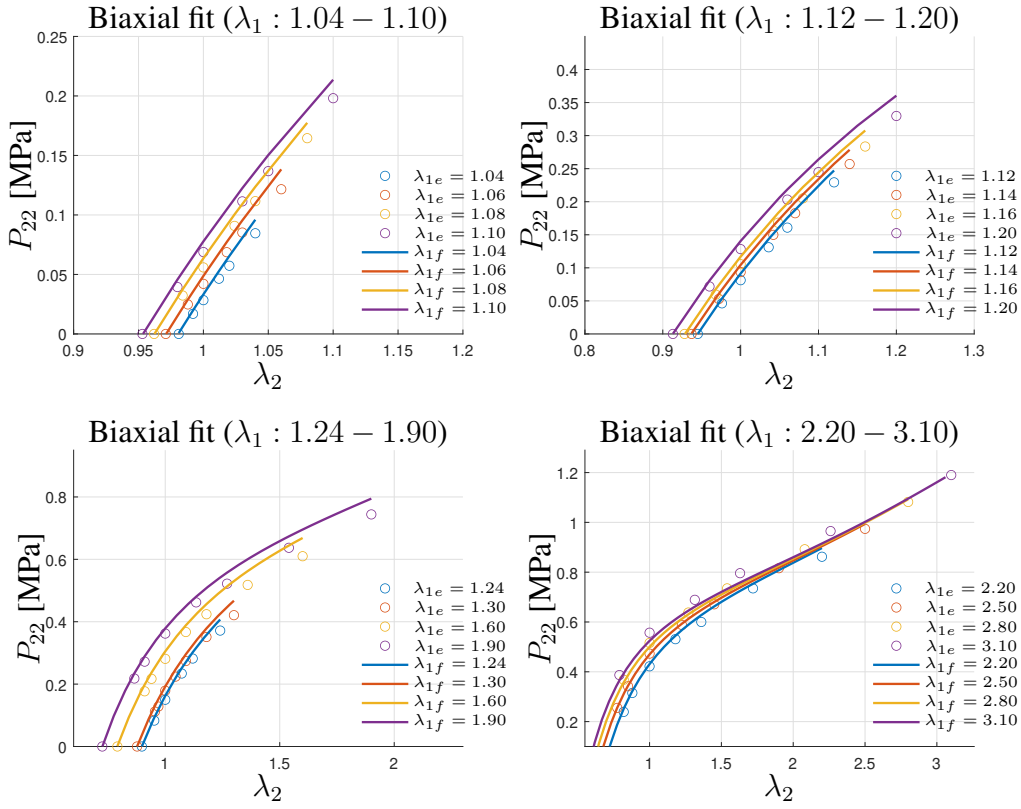

Figure 4.15: Principal stretch based model predictions for Kawabata data

Table 4.12: Principal stretch-based approach: Vertices fitted to Kawabata data

p_1	0.007309	p_7	0.873982
p_2	0.770354	p_8	0.945474
p_3	0.796691	p_9	1.026919
p_4	0.796988	p_{10}	1.123305
p_5	0.797273	p_{11}	1.225094
p_6	0.804144	p_{12}	1.358111

4.8 Modified Principal Stretch Based Approach(Ogden-like Approach)

Similar to principal stretch based approach the free energy function is assumed to be function of principal stretches.

4.8.1 Methodology

As done in the previous principal stretch based approach, stress tensor can be defined as;

$$\boxed{\begin{aligned}\mathbf{S} &= \sum_{a=1}^{3} \frac{1}{\lambda_a}\beta_a \mathbf{N}_a \otimes \mathbf{N}_a - p\mathbf{C}^{-1} \\ \boldsymbol{\tau} &= \sum_{a=1}^{3} \lambda_a \beta_a \mathbf{n}_a \otimes \mathbf{n}_a - p\mathbf{1}\end{aligned}} \tag{4.24}$$

with

$$\beta_1 = \frac{\partial \psi}{\partial \lambda_1} \quad \beta_2 = \frac{\partial \psi}{\partial \lambda_2} \quad \beta_3 = \frac{\partial \psi}{\partial \lambda_3} \tag{4.25}$$

where $\beta_a = \frac{\partial \psi}{\partial \lambda_a}$ with a=1,2,3 and replaced by B-spline

$$\beta_a = \frac{\partial \psi}{\partial \lambda_a} = \begin{bmatrix} N_{1,1}(\lambda_a) & \cdots & N_{1,n}(\lambda_a) \end{bmatrix} \begin{pmatrix} \hat{P}_1 \\ \vdots \\ \hat{P}_n \end{pmatrix} \tag{4.26}$$

Since the principal stretch based model is not performing well, additional terms are needed the increase its performance. This operation is a pretty similar process as in Ogden's model [19] this method can be considered as an Ogden-like model. We can redefine $\boldsymbol{\tau}$ expression as;

$$\boldsymbol{\tau} = \sum_{a=1}^{3} (\lambda_a \beta_a \mathbf{n}_a \otimes \mathbf{n}_a + \lambda_a \frac{\partial \psi}{\partial \nu_a} \frac{\partial \nu_a}{\partial \lambda_a} \mathbf{n}_a \otimes \mathbf{n}_a) - p\mathbf{1} \tag{4.27}$$

where

$$\nu_a = \frac{1}{\lambda_a}, \qquad \frac{\partial \nu_a}{\partial \lambda_a} = -\frac{1}{\lambda_a^2} \tag{4.28}$$

reads

$$\boldsymbol{\tau} = \sum_{a=1}^{3} (\lambda_a \beta_a \mathbf{n}_a \otimes \mathbf{n}_a - \frac{1}{\lambda_a} \gamma_a(\nu_a) \mathbf{n}_a \otimes \mathbf{n}_a) - p\mathbf{1} \tag{4.29}$$

$$\gamma_a = \frac{\partial \psi}{\partial \nu_a} = \begin{bmatrix} N_{2,1}(\lambda_a) & \cdots & N_{2,n}(\lambda_a) \end{bmatrix} \begin{pmatrix} \hat{P}_1 \\ \vdots \\ \hat{P}_n \end{pmatrix} \tag{4.30}$$

4.8.2 Results for Modified Principal Stretch Based Approach

Treloar and Kawabata data sets are employed to evaluate the performance of the modified principal stretch based approach.

4.8.2.1 Treloar Based Simultaneous Fit Results

The simultaneous model predictions of modified principal stretch based approach for Treloar data is shown in Figure 4.16. In this fit, all experiments are simultaneously included in the optimization problem; also weights of all data are included in this optimization problem. Values of the weight distribution can be seen in Table 4.15.

The additional term has given the model flexibility to fit the test data in the non-Gaussian region.

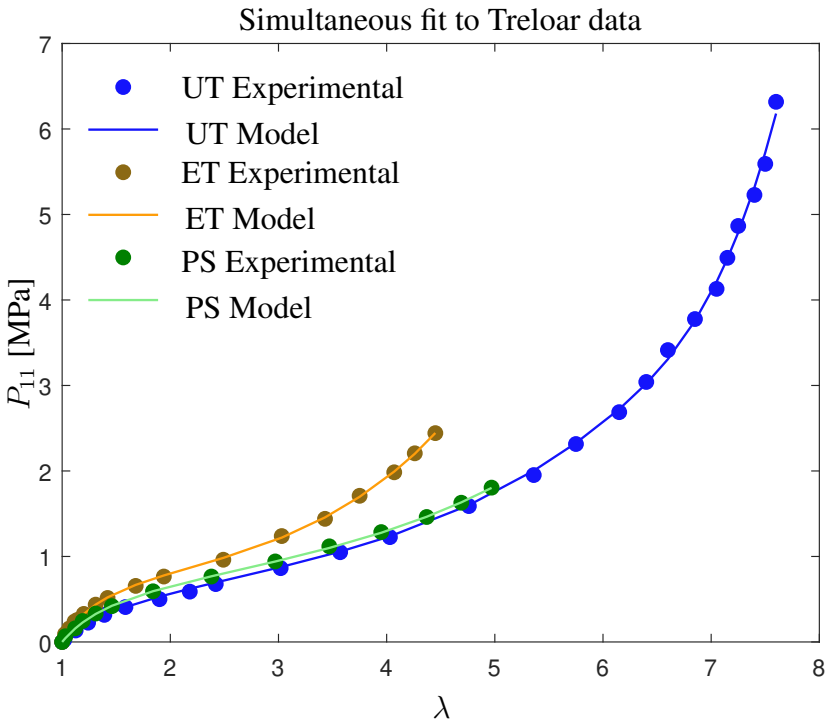

Figure 4.16: Modified principal stretch based approach fitted to Treloar data simultaneously

In Table 4.13, control point values calculated through optimization are shown. The optimized values also obey the stability constraint rules shown in 4.2.

Table 4.13: Modified principal stretch based approach: Vertices fitted to Treloar data

	$\hat{c}_1$	$\hat{c}_2$
p_1	0.084193	0.033827
p_2	0.530532	0.068994
p_3	0.536627	0.074366
p_4	0.865464	0.078333
p_5	1.420563	0.124170
p_6	2.971365	0.184306
p_7	6.160343	0.254215
p_8	46.46855	0.420333

By using the same vertices, model performance is check also for the Kawabata tests, see Figure 4.17. It is seen that the vertices found from Trealor fit works also quite nicely for the Kawabata data except for the tests with greater than $\lambda_1 = 2.5$.

Table 4.14: Modified principal stretch based approach: QOF values for Treloar data

	Region 1	Region 2	Region 3
UT	0.0050	0.0059	0.0218
ET	0.0182	0.0192	0.0198
PS	0.0087	0.0088	0.0092
ALL	0.0320	0.0340	0.0509

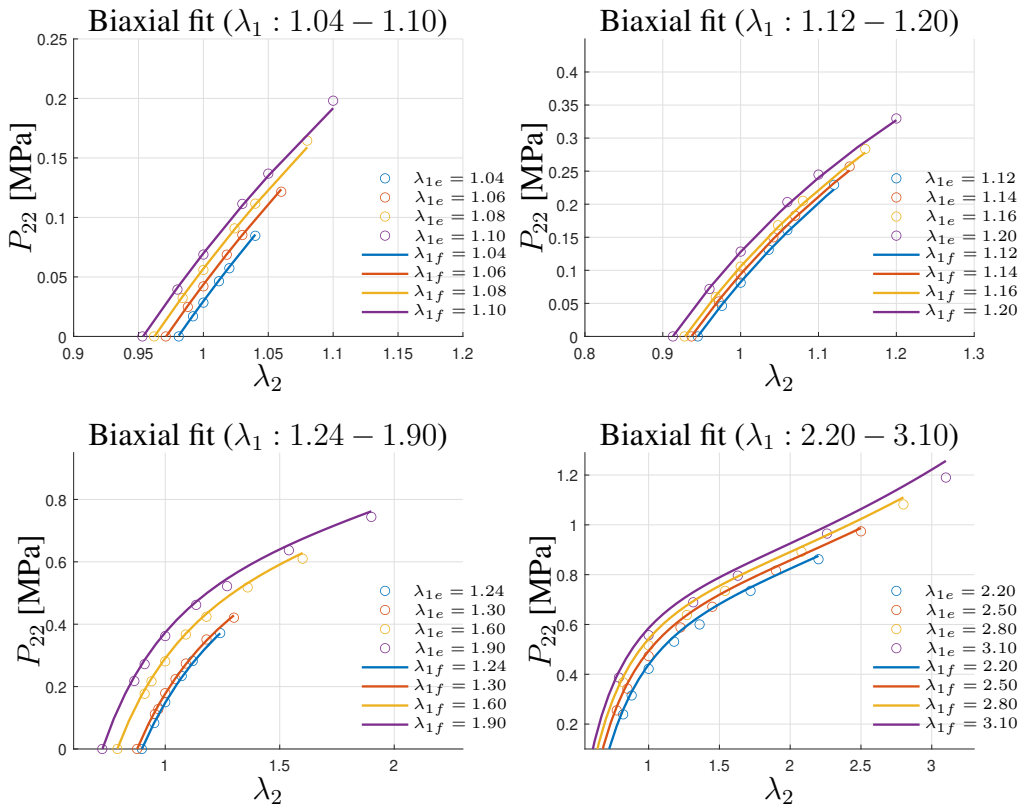

Figure 4.17: Modified Principal stretch based model predictions (Kawabata data/Treloar Fit results)

Table 4.15: Modified principal stretch-based approach: Weights fitted to Treloar data

	w_{ut}	w_{et}	w_{ps}
weights	0.20	0.20	0.60

4.8.2.2 Kawabata Based Biaxial Fit Results

The modified principal stretch based model is also validated with Kawabata data. All fits are done with the same number of control points and degrees with the Treloar data fit to make it easy to compare Fitted results can be seen in Figure 4.18, and the vertice sets are given in Table 4.16

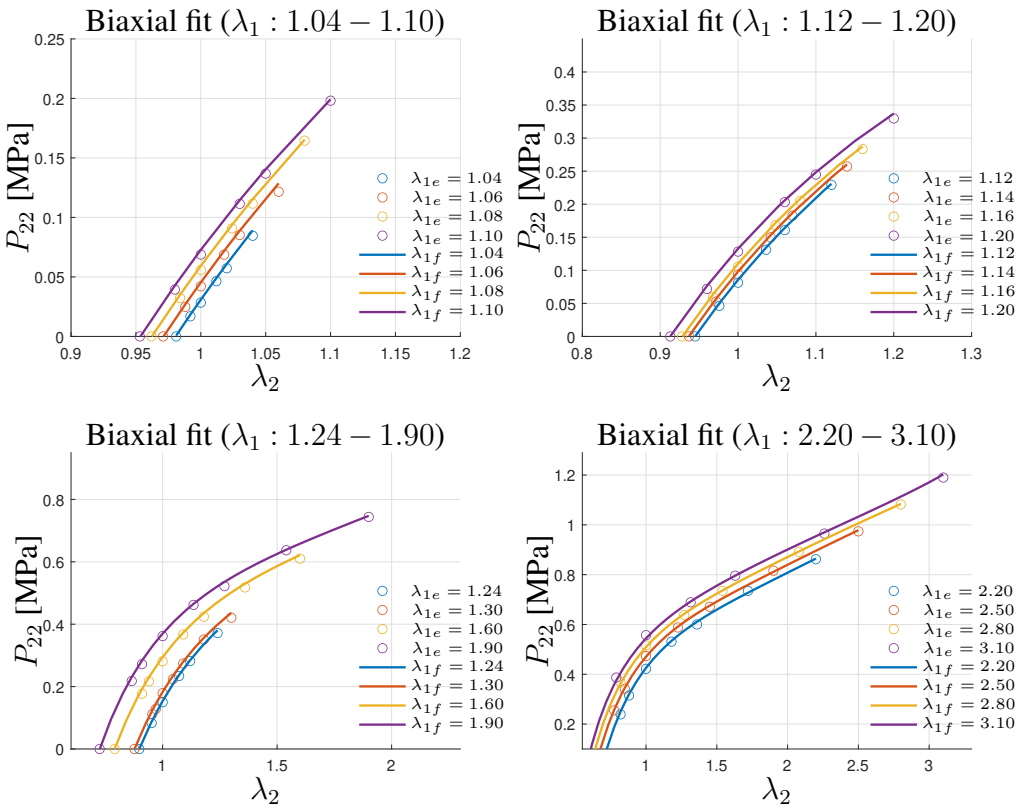

Figure 4.18: Modified Principal stretch based model predictions (Kawabata data/Kawabata fit results)

Table 4.16: Modified principal stretch based approach: Vertices fitted to Treloar data

	$\hat{c}_1$	$\hat{c}_2$
p_1	0.023130	0.002882
p_2	0.043360	0.005845
p_3	0.583708	0.007009
p_4	0.656359	0.033689
p_5	0.825263	0.057258
p_6	1.044102	0.059039
p_7	1.184615	0.072957
p_8	5.973244	0.148117

Using vertice sets of Kawabata fit, model performance is also checked for the Treloar data, see Figure 4.19. Since the stretch range of Kawabata data is less than Treloar,

model success is not good where $\lambda > 2.5$.

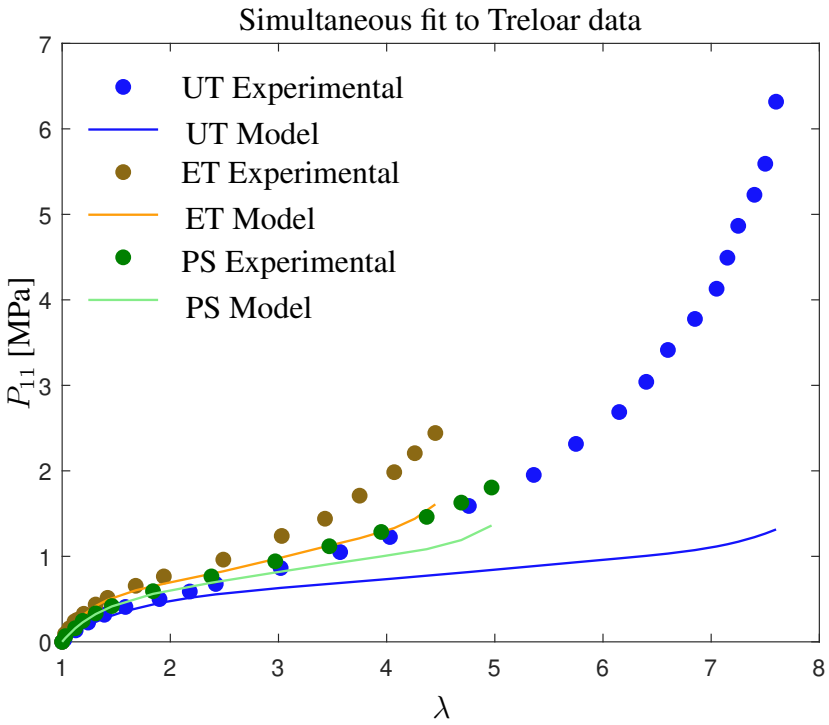

Figure 4.19: Modified principal stretch based model predictions for Treloar data from vertice points obtained from Kawabata data

4.9 Effect of Stability Constraint

As defined in 4.1, constraints are needed to obtain meaningful results and to focus on physical meaning while generating data-driven models. Constraints decrease the solution interval of the models and sometimes complicate the fitting but also provide physically consistent models. As shown in Figure 4.20a and 4.20b, constraints add smoothness to the model results.

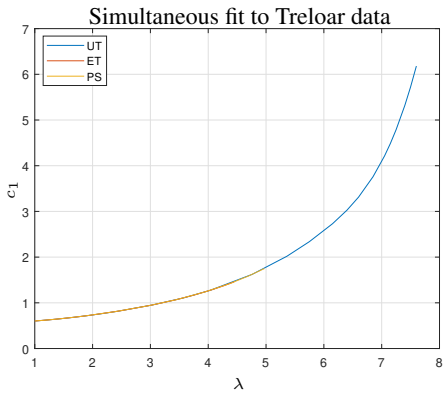

(a) c_1 vs. λ graph for modified principal stretch based model with stability constraint

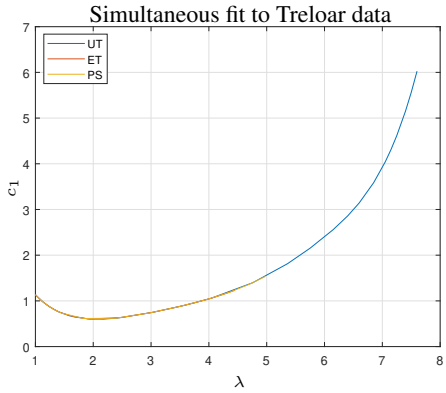

(b) c_1 vs. λ graph for the modified principal stretch based model without stability constraint

Figure 4.20: Derivatives of energy function with respect to stretch values

As given in Table 4.17 the model's performance is decreasing with constraints as expected, but physically reliable method generation is the primary goal of the models.

Table 4.17: Principal stretch-based approach: Weights fitted to Treloar data

	With constraint	Without constraint
Error	0.050915	0.048052

In this thesis, four different data-driven model approaches are mentioned, and three of them give satisfactory results in the interval where the model has input test data. B-Spline functions in all approaches are generated only for existing ranges in tests. Since B-Spline is not generated beyond these limits, the model does not perform well beyond limits. This can be easily seen in Figures 4.7, 4.12, and 4.19 where the Treloar fits are performed with the vertices of Kawabata fits. The uniaxial tension test has a stretch range between $1 - 7.6$, and the biaxial tension test has a stretch range for λ_1 between $1.04 - 3.1$. When vertices from simultaneous fits of Treloar data are used for Kawabata fits, BE fits are not perfect but not very far away from the exact behavior of the material, see Figures 4.5, 4.10 and 4.17. On the other hand, BE fit results are not working correctly with Treloar data since the data limit is out of range.

4.10 Effect of Vertice Number

In order to see the effect of the control point (vertice) number on the quality of fit, an additional study is conducted by using the modified invariant based approach. It is expected that as the vertice number increases, the accuracy of the fit should also increase. However, the main purpose of the study is to determine an appropriate number for the vertices that should be used in the model. For this study, only the Treloar data sets are employed, and the quality of fits are determined from the simultaneous fits to Treloar data.

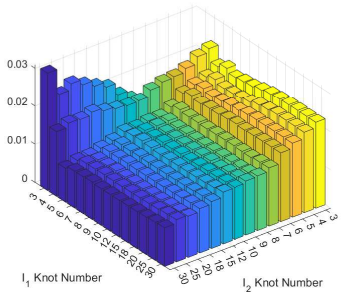

(a) Quality of fit comparison for region 1

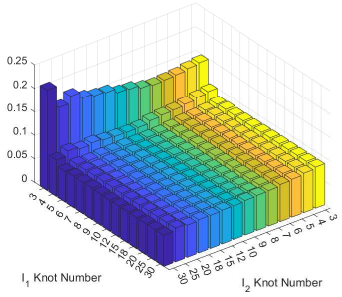

(b) Quality of fit comparison for region 2

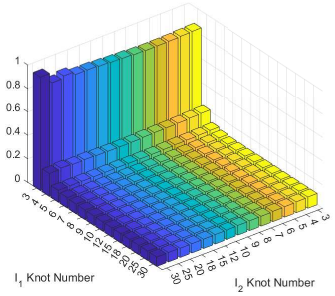

(c) Quality of fit comparison for region 3

Figure 4.21: Vertice number effect for modified invariant based approach

Figure 4.21 shows the effect of vertice number on the quality of fit for 3 different regions. The effect of vertice number is much greater in the first region, for the other two regions fit quality changes significantly at the beginning but later remains almost constant as the vertice number increases. If we compare the effect of knot number in the case of I_1 and I_2, we can say that I_1 is the main invariant that has the bigger

effect on the response of the material. Thus, increasing the vertice number of the B-spline responsible for I_1 affects the quality of fit more. On the other hand, the effect of I_2 can be seen in region one since area change has more effect for smaller stretch values, as the material elongates the chains in the rubber get aligned. Then, in higher stretches area change becomes less important compared to chain elongations.

4.11 Effect of Degree of Polynomial

Another study was conducted to observe and validate the effect of basis function degree (or B-spline order) on the quality of fit. The vertice number is fixed to 20 and the order of the B-spline is increased. The study is done for the modified invariant based approach.

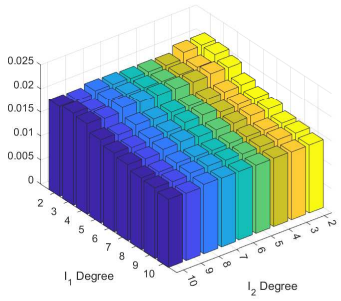

(a) Quality of fit comparison for region 1

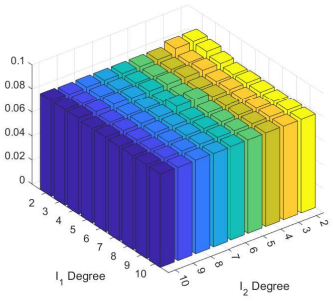

(b) Quality of fit comparison for region 2

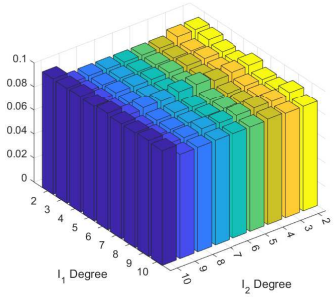

(c) Quality of fit comparison for region 3

Figure 4.22: Degree effect for modified invariant based approach

As shown in Figure 4.22 except region 1, for the other two regions increasing the degree of the basis function has nearly no effect on the quality of fit criteria. If we are

using enough vertices, there is no need to use higher degree basis functions, we can say that degree 2 may be sufficient.

CHAPTER 5

CONCLUSIONS

In this study, four data-driven models for rubberlike materials have been proposed, and a generalized parametric spline generation tool has been developed. The performance of all models has been observed, and the ways to increase their performance has investigated.

Two of the models are assumed to have free energy functions that are functions of the material invariants, and the other two approaches are assumed to be based on principal stretches. However, the common point for all proposed models is to create a model with the help of partial derivatives of the free energy function without defining the free energy function itself. The main idea of this work was not to be forced to define any free energy function and to be able to define a general data-driven hyperelastic model which can be used for all rubberlike materials. When the performances of these four different approaches are compared, we can say that modified invariant and modified stretch based models are the two best approaches, followed by invariant based and stretch based models, respectively. We can first examine the modified invariant-based approach to understand the reason for this. Unlike the invariant based approach, we can see that the effects of longitudinal elongation and areal changes are reflected much more realistically in the modified invariant based approach. When the derivative functions of the model are examined, it is seen that the effect of I_2 decreases gradually when high stretch levels are reached, as expected, but the same cannot be said for the invariant based approach. For the case of the modified principal stretch based approach, the term $\nu_a = \frac{1}{\lambda_a}$, which was later added to the model, both increased the flexibility of the model and, in a sense, enabled the model to take into account the effects of surface area changes that are perpendicular to the direction of the principal

stretch as shown in Figure 2.3. While the modified stretch-based approach has very impressive results, the modified invariant-based approach gives slightly better results with our optimization method. If another optimization method had been used, perhaps the opposite would have happened.

Additionally, the effect of control points and basis function degrees is investigated for all models. Since the test data is not very complex, B-spline curves of lower order can also solve the problem with very similar performance compared to higher order ones. On the other hand, the effect of the number of control points is more significant, but we can say that by observation, the user does not have to increase the number of the control points too much to get a satisfactory result. This process can be optimized by a residual approach to understanding how things work. If the outcome doesn't change, there is no need to use too many control points.

Three of the models give satisfactory results in the interval where the model has input test data. B-Spline functions in all approaches are generated only for existing ranges in tests. Since B-Spline is not generated beyond these limits, the model does not perform well beyond limits. This can be easily seen in Figures 4.7, 4.12, and 4.19, where the Treloar fits are performed with the vertices of Kawabata fits. The uniaxial tension test has a stretch range between $1 - 7.6$, and the biaxial tension test has a stretch range for λ_1 between $1.04 - 3.1$. When vertices from simultaneous fits of Treloar data are used for Kawabata fits, BE fits are not perfect but not very far away from the exact behavior of the material, see Figures 4.5, 4.10 and 4.17. On the other hand, BE fit results are not working correctly with Treloar data since the data limit is out of range. A basic extrapolation algorithm should be added for the out-of-range predictions to avoid this for future FE implementations of the method.

In the literature, numerous models were proposed to get a constitutive response for rubberlike materials. These models are also based on some optimization of parameters defined by the model owner. However, most of them have the more likely physical definition. By this approach, the data-driven model has more fundamental physics, so the model can be extended and might have more common future applications. Since the $basisvector$ tool is generalized and parameterized, it might be used in the near future for any academic or industrial study.

As a solver from MATLAB's Optimization Toolbox, FMINCON was selected. FMINCON requests the initial optimization point to calculate the results. These initial points can be assigned with a genetic algorithm. However, the problem is that the genetic algorithm is giving better results with fewer parameters. Since, with a data-driven model, we need to solve equations for more than five parameters and be constrained with physical meanings, a genetic solver is not a good choice for this method.

Throughout the study, physical consistency is always considered in order to maintain repeatability. Mathematical constraints support this consistency in the optimization solver FMINCON by MATLAB. Linear inequality constraints are applied to get a more accessible and accurate result.

With only a single tool, four different models have been introduced at the first approach, the number of approaches will increase soon, and the data-driven approach will help to get more successful computations for engineering problems with less effort.

The results of the study are auspicious. For future work, results can be run in finite element solvers to investigate the validation of the approach on the structural level. On the other hand, extrapolation studies and different material investigations can be conducted. A data-driven model can be applied to any data that is hard to solve or needs to be optimized.

REFERENCES

[1] H. Dal, K. Açıkgöz, and Y. Badienia, "On the performance of isotropic hyperelastic constitutive models for rubber-like materials: A state of the art review." *Applied Mechanics Reviews*, vol. 73, p. 020802, 2021.

[2] A. Gent, *Engineering with rubber*. Hanser, 2012.

[3] J. E. Mark and B. Erman, *Rubberlike elasticity a molecular primer*. Cambridge University Press, 2007.

[4] F. E. Bock, R. C. Aydin, C. J. Cyron, N. Huber, S. R. Kalidindi, and B. Klusemann, "A review of the application of machine learning and data mining approaches in continuum materials mechanics," *Frontiers in Materials*, vol. 6, p. 110, 2019.

[5] A. Ghaderi, V. Morovati, and R. Dargazany, "A physics-informed assembly of feed-forward neural network engines to predict inelasticity in cross-linked polymers," *Polymers*, vol. 12, no. 11, p. 2628, 2020.

[6] T. Kirchdoerfer and M. Ortiz, "Data-driven computational mechanics," *Computer Methods in Applied Mechanics and Engineering*, vol. 304, pp. 81–101, 2016.

[7] L. T. K. Nguyen and M.-A. Keip, "A data-driven approach to nonlinear elasticity," *Computers & Structures*, vol. 194, pp. 97–115, 2018.

[8] R. Eggersmann, T. Kirchdoerfer, S. Reese, L. Stainier, and M. Ortiz, "Model-free data-driven inelasticity," *Computer Methods in Applied Mechanics and Engineering*, vol. 350, pp. 81–99, 2019.

[9] T. Sussman and K.-J. Bathe, "A model of incompressible isotropic hyperelastic material behavior using spline interpolations of tension–compression test data," *Communications in numerical methods in engineering*, vol. 25, no. 1, pp. 53–63,

2009.

[10] V. Amores, J. Benitez, and F. Montáns, "Average-chain behavior of isotropic incompressible polymers obtained from macroscopic experimental data. a simple structure-based wypiwyg model in julia language." *Advanced Engineering Software*, vol. 130, pp. 41–57, 2019.

[11] V. J. Amores, J. M. Benítez, and F. J. Montáns, "Data-driven, structure-based hyperelastic manifolds: A macro-micro-macro approach to reverse-engineer the chain behavior and perform efficient simulations of polymers," *Computers Structures*, vol. 231, p. 106209, 2020.

[12] L. R. Treloar, "The elasticity of a network of long-chain molecules—ii," *Trans. Faraday Soc.*, vol. 39, p. 241–246, 1943.

[13] O. H. Yeoh, "Characterization of elastic properties of carbon-black-filled rubber vulcanizates," *Rubber Chemistry and Technology*, vol. 63, no. 5, p. 792–805, 1990.

[14] A. N. Gent, "A new constitutive relation for rubber," *Rubber Chemistry and Technology*, vol. 69, no. 1, p. 59–61, 1996.

[15] O. H. Yeoh and P. D. Fleming, "A new attempt to reconcile the statistical and phenomenological theories of rubber elasticity," *Journal of Polymer Science Part B: Polymer Physics*, vol. 35, no. 12, p. 1919–1931, 1997.

[16] M. Mooney, "A theory of large elastic deformation," *Journal of Applied Physics*, vol. 11, no. 9, p. 582–592, 1940.

[17] R. S. Rivlin, "Large elastic deformations of isotropic materials iv. further developments of the general theory," *Philosophical Transactions of the Royal Society of London. Series A, Mathematical and Physical Sciences*, vol. 241, no. 835, p. 379–397, 1948.

[18] K. C. Valanis and R. F. Landel, "The strain-energy function of a hyperelastic material in terms of the extension ratios," *Journal of Applied Physics*, vol. 38, no. 7, p. 2997–3002, 1967.

[19] R. W. Ogden, "Large deformation isotropic elasticity—on the correlation of theory and experiment for incompressible rubberlike solids," *Rubber Chemistry and Technology*, vol. 46, no. 2, p. 398–416, 1973.

[20] M. H. Shariff, "Strain energy function for filled and unfilled rubberlike material," *Rubber Chemistry and Technology*, vol. 73, no. 1, p. 1–18, 2000.

[21] G. Heinrich and M. Kaliske, "Theoretical and numerical formulation of a molecular based constitutive tube-model of rubber elasticity," *Computational and Theoretical Polymer Science*, vol. 7, no. 3-4, p. 227–241, 1997.

[22] M. C. Wang and E. Guth, "Statistical theory of networks of non-gaussian flexible chains," *The Journal of Chemical Physics*, vol. 20, no. 7, p. 1144–1157, 1952.

[23] E. M. Arruda and M. C. Boyce, "A three-dimensional constitutive model for the large stretch behavior of rubber elastic materials," *Journal of the Mechanics and Physics of Solids*, vol. 41, no. 2, p. 389–412, 1993.

[24] C. Miehe and S. Göktepe, "A micro-macro approach to rubber-like materials?part i: The non-affine micro-sphere model of rubber elasticity," *Journal of the Mechanics and Physics of Solids*, vol. 52, no. 11, p. 2617–2660, 2004.

[25] M. C. Boyce and E. M. Arruda, "Constitutive models of rubber elasticity: A review," *Rubber Chemistry and Technology*, vol. 73, no. 3, p. 504–523, 2000.

[26] P. J. Flory and B. Erman, "Theory of elasticity of polymer networks. 3," *Macromolecules*, vol. 15, no. 3, p. 800–806, 1982.

[27] L. R. Treloar, "Stress-strain data for vulcanized rubber under various types of deformation," *Rubber Chemistry and Technology*, vol. 17, no. 4, p. 813–825, 1944.

[28] S. Kawabata, M. Matsuda, K. Tei, and H. Kawai, "Experimental survey of the strain energy density function of isoprene rubber vulcanizate," *Macromolecules*, vol. 14, no. 1, p. 154–162, 1981.

[29] P. J. Flory, "Thermodynamic relations for high elastic materials," *Transactions of the Faraday Society*, vol. 57, p. 829, 1961.

[30] R. Ogden, "Elastic deformations of rubberlike solids," *Mechanics of Solids*, p. 499–537, 1982.

[31] C. Miehe, "Aspects of the formulation and finite element implementation of large strain isotropic elasticity," *International Journal for Numerical Methods in Engineering*, vol. 37, no. 12, p. 1981–2004, 1994.

[32] M. Kaliske and H. Rothert, "Formulation and implementation of three-dimensional viscoelasticity at small and finite strains," *Computational Mechanics*, vol. 19, no. 3, p. 228–239, 1997.

[33] C. Miehe, "Superimposed finite elastic–viscoelastic–plastoelastic stress response with damage in filled rubbery polymers. experiments, modelling and algorithmic implementation," *Journal of the Mechanics and Physics of Solids*, vol. 48, no. 2, p. 323–365, 2000.

[34] J. Simo, R. Taylor, and K. Pister, "Variational and projection methods for the volume constraint in finite deformation elasto-plasticity," *Computer Methods in Applied Mechanics and Engineering*, vol. 51, no. 1-3, p. 177–208, 1985.

[35] H. Dal, O. Gültekin, and K. Açıkgöz, "An extended eight-chain model for hyperelastic and finite viscoelastic response of rubberlike materials:theory, experiments and numerical aspects." *J. Mech. Phys. Solids*, vol. 145, p. 104159, 2020.

[36] H. Dal, B. Cansiz, and C. Miehe, "A three-scale compressible microsphere model for hyperelastic materials," *International Journal for Numerical Methods in Engineering*, vol. 116, no. 6, p. 412–433, 2018.

[37] C. Kadapa and M. Hossain, "A linearized consistent mixed displacement-pressure formulation for hyperelasticity," *Mechanics of Advanced Materials and Structures*, vol. 29, no. 2, p. 267–284, 2020.

[38] C. de Boor, "Good approximation by spline with variable knots ii," *Lect Notes Math*, vol. 363, 01 1974.

[39] H. Dal, K. Acikgoz, and Y. Badienia, "On the performance of isotropic hyperelastic constitutive models for rubber-like materials: A state of the art review,"

APPENDIX A

MATLAB CODE FOR B-SPLINE

- nok(integer) : Number of knots
- xin(array) : Solution domain ($x - axis$)
- order(integer): Order of shape function
- plotcheck(logical): true(generates plots for shape functions to check them)

```
function [N,del,xinkg,knotxinoriginal,Nfull,xfull,knotfull]=...
    basisvector(nok,xin,order,plotcheck)
   Defining
format longE
tol=eps(10000);
noel=50;
nok=nok 1;
xinkf=linspace(xin(1),xin (end),nok noel+1);
knotloc=zeros(floor(length(xinkf)/noel)+1,1);
for i=1:length(knotloc)
    knotloc(i)=1+noel (i 1);
end
knotxin=zeros(length(knotloc),1);
for i=1:length(knotloc)
    knotxin(i)=xinkf(knotloc(i));
end
knotxinoriginal=knotxin;
   Data adjustment
del=knotxin(2) knotxin(1);
xink=linspace(xin(1) del order,xin (end)+del order,((nok+2 order) noel+1));
for i=1:length(xink)
```

```
22      for j=1:length(xin)
23          if abs(xink(i) xin(j)) tol
24              xink(i)=xin(j);
25          end
26      end
27  end
28  knotloc=zeros(floor(length(xink)/noel)+1,1);
29  for i=1:length(knotloc)
30      knotloc(i)=1+noel (i 1) ; knot index in variables
31  end
32  knotxin=zeros(length(knotloc),1); knot values
33  for i=1:length(knotloc)
34      knotxin(i)=xink(knotloc(i));
35  end
36  xink=[xink, xin];
37  xink=sort(unique(xink));
38  for k=1:length(knotloc)
39         knotloc(k)=find(xink==knotxin(k));
40  end
41     Calculation of Basis Vector
42  N=zeros(order,length(xink),length(knotxin) 1+2 order+2);
43  for i=order+1:length(knotxin)+order 1
44      for j=knotloc(i order):knotloc(i+1 order) 1
45          N(1,j,i)=1;
46      end
47  end
48  for d=2:order
49      for i=1:(length(knotxin)) d
50          for k=1:length(xink) 1
51              N(d,k,i+order)=(((xink(k) knotxin(i))/(knotxin(i+d 1) ...
52                   knotxin(i)) N(d 1,k,i+order)))+(((knotxin(i+d)  ...
53                  xink(k))/(knotxin(i+d) knotxin(i+1)) ...
54                   N(d 1,k,i+1+order)));
55          end
56      end
57  end
58  Nfull=N;
59  xfull=xink;
60  knotfull=knotxin;
61    Result arranging
```

```
xinkg=xink(knotloc(1+order):knotloc(end order));
xinkg=sort(unique(xinkg));
Nend=zeros(order,length(xinkg),nok+2);
nstart=knotloc(1+order);
nend=knotloc(end order);
for d=1:order
    for i=1:nok+order+1
        count=0;
        for k=nstart:nend
            count=count+1;
            Nend(d,count,i)=N(d,k,i+order);
        end
    end
end
N=Nend;
   Plot
if plotcheck==true
    for i=1:order
        figure
        xlabel( x )
        ylabel( y )
        title( T )
        hold on
        grid minor
        for k=1:size(N,3)
            plot(xinkg,N(i,:,k))
        end
        legend( Location , eastoutside )
    end
end
end
```

APPENDIX B

QOF RESULTS FOR NON-SIMULTANEOUS CASES

a Effect of Knot Number for UT Only Fit

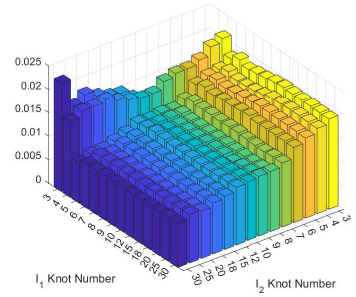

(a) Quality of fit comparison for region 1

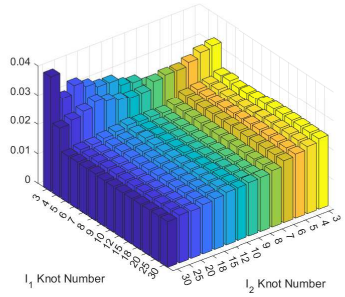

(b) Quality of fit comparison for region 2

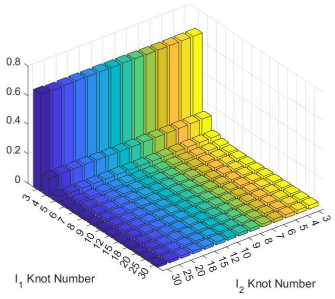

(c) Quality of fit comparison for region 3

Figure B.1: Knot effect on UT for modified invariant based approach

b Effect of Degree for UT Only Fit

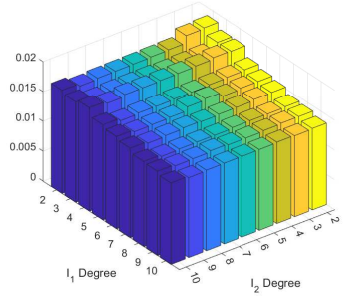

(a) Quality of fit comparison for region 1

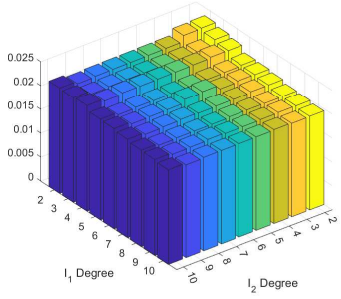

(b) Quality of fit comparison for region 2

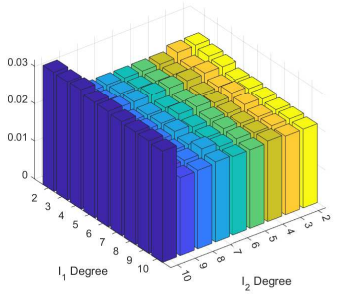

(c) Quality of fit comparison for region 3

Figure B.2: Degree effect on UT for modified invariant based approach

c Effect of Knot Number for ET Only Fit

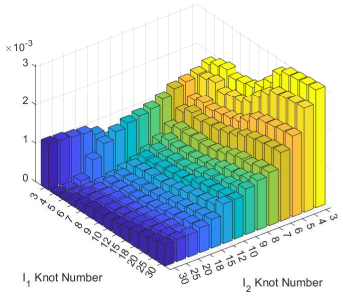

(a) Quality of fit comparison for region 1

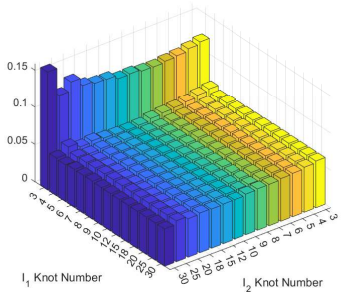

(b) Quality of fit comparison for region 2

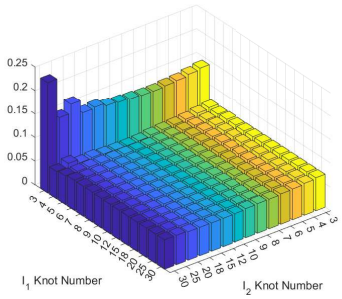

(c) Quality of fit comparison for region 3

Figure B.3: Knot effect on ET for modified invariant based approach

d Effect of Degree for ET Only Fit

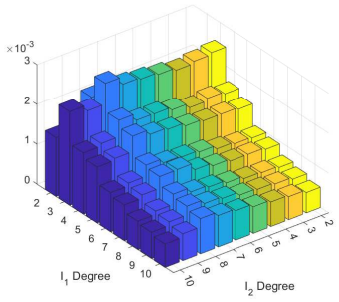

(a) Quality of fit comparison for region 1

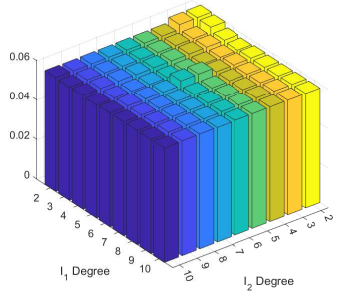

(b) Quality of fit comparison for region 2

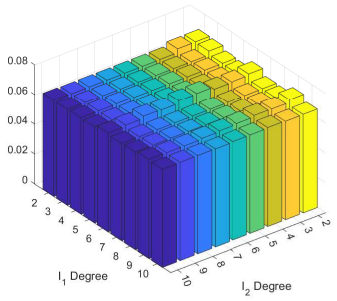

(c) Quality of fit comparison for region 3

Figure B.4: Degree effect on ET for modified invariant based approach

e Effect of Knot Number for PS Only Fit

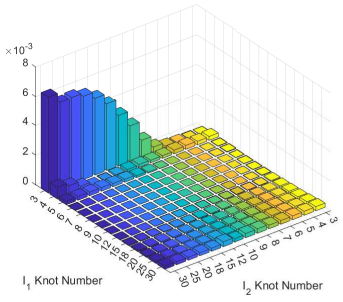

(a) Quality of fit comparison for region 1

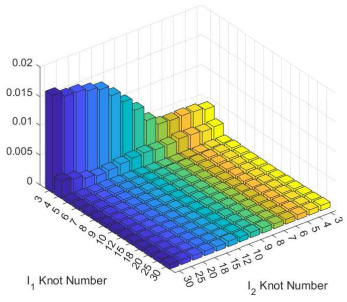

(b) Quality of fit comparison for region 2

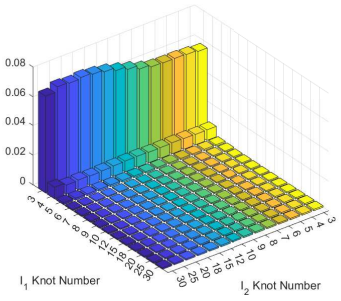

(c) Quality of fit comparison for region 3

Figure B.5: Knot effect on PS for modified invariant based approach

f Effect of Degree for PS Only Fit

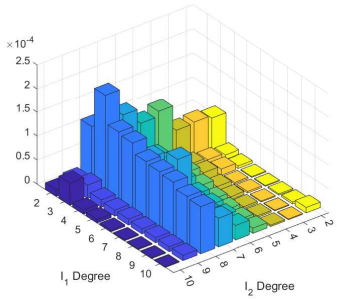

(a) Quality of fit comparison for region 1

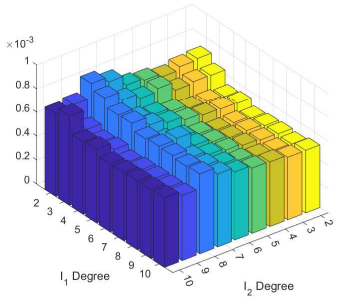

(b) Quality of fit comparison for region 2

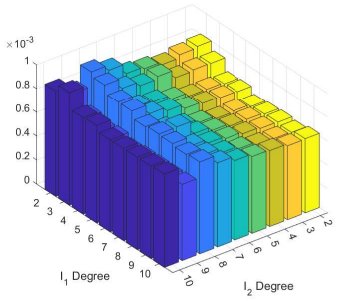

(c) Quality of fit comparison for region 3

Figure B.6: Degree effect on PS for modified invariant based approach